

Development of a Particle Flux Detection System for the MERIT High-Intensity Target Experiment at CERN

I. Efthymiopoulos, A. Fabich, M. Palmⁱ

Abstract

The construction of a high intensity neutrino source requires multi megawatt beams and challenges the targets in use. MERIT is a proof-of-principle test for a novel kind of neutrino factory target, employing a 24 GeV/c proton beam and a 1-cm in diameter free mercury jet as beam target. This thesis describes the design and implementation of a secondary particle flux production detection system. Employed detectors are polycrystalline diamond detectors and electron multipliers. Simulations of the secondary particle production have been made using FLUKA. The detection system is remotely controlled by a LabView interface and experimental observations from the initial analysis are presented.

ⁱ Diploma Thesis work of Marcus Palm, submitted to Linköpings Universitet, 581 83 Linköping – Sweden

Institutionen för fysik, kemi och biologi

Examensarbete

**Development of a particle flux detection system for
the MERIT high intensity target experiment at
CERN**

Marcus Palm

LITH-IFM-EX--08/1951--SE



Linköpings universitet
TEKNISKA HÖGSKOLAN

Institutionen för fysik, kemi och biologi
Linköpings universitet
581 83 Linköping

Examensarbete
LITH-IFM-EX--08/1951--SE


**Development of a particle flux detection system for
the MERIT high intensity target experiment at
CERN**

Marcus Palm

Handledare: **Ilias Eftymiopoulos**
AB/ATB/SBA, CERN
Rolf Riklund
IFM, Linköpings Universitet
Peter Münger
IFM, Linköpings Universitet

Examinator: **Peter Münger**
IFM, Linköpings universitet

Linköping, 17 May, 2008

	Avdelning, Institution Division, Department Division of Applied Physics Department of Physics, Chemistry and Biology Linköpings universitet SE-581 83 Linköping, Sweden		Datum Date 2008-05-17
	Språk Language <input type="checkbox"/> Svenska/Swedish <input checked="" type="checkbox"/> Engelska/English <input type="checkbox"/> _____	Rapporttyp Report category <input type="checkbox"/> Licentiatavhandling <input checked="" type="checkbox"/> Examensarbete <input type="checkbox"/> C-uppsats <input type="checkbox"/> D-uppsats <input type="checkbox"/> Övrig rapport <input type="checkbox"/> _____	ISBN _____ ISRN LITH-IFM-EX--08/1951--SE Serietitel och serienummer ISSN Title of series, numbering _____
URL för elektronisk version http://www.ep.liu.se			
Titel Development of a particle flux detection system for the MERIT high intensity Title target experiment at CERN			
Författare Marcus Palm Author			
Sammanfattning Abstract <p>The construction of a high intensity neutrino source requires multi megawatt beams and challenges the targets in use. MERIT is a proof-of-principle test for a novel kind of neutrino factory target, employing a 24 GeV/c proton beam and a 1 cm in diameter free mercury jet as beam target. This thesis describes the design and implementation of a secondary particle flux production detection system. Employed detectors are polycrystalline diamond detectors and electron multipliers. Simulations of the secondary particle production have been made using FLUKA. The detection system is remotely controlled by a LabView interface and experimental observations from the initial analysis are presented.</p>			
Nyckelord Keywords diamond, particle, detectors, neutrino, factory, mercury, jet, CERN			

Abstract

The construction of a high intensity neutrino source requires multi megawatt beams and challenges the targets in use. MERIT is a proof-of-principle test for a novel kind of neutrino factory target, employing a 24 GeV/c proton beam and a 1 cm in diameter free mercury jet as beam target. This thesis describes the design and implementation of a secondary particle flux production detection system. Employed detectors are polycrystalline diamond detectors and electron multipliers. Simulations of the secondary particle production have been made using FLUKA. The detection system is remotely controlled by a LabView interface and experimental observations from the initial analysis are presented.

Acknowledgments

I want to express my sincere gratitude to my supervisor Ilias Efthymiopoulos for his skillful and experienced guidance, innumerable valuable advices on large and small subjects and inspiring confidence in my work throughout my time at CERN.

Many thanks to Adrian Fabich for rewarding discussions and his help in many practical questions.

A special thanks to Heinz Pernegger, for his dedicated and invaluable work with the diamond measurements and detector assembly.

I would also like to thank Rolf Riklund for recommending me to apply to a Technical Student position at CERN in the first place and my university supervisor Peter Munger for his help with putting this thesis together.

A warm thanks to all my friends who added splendor to the Franco-Swiss living at and outside CERN.

Contents

1	Introduction	1
1.1	CERN	1
1.2	MERIT	3
2	Problem definition	5
3	MERIT description	7
3.1	Experimental setup	7
3.1.1	Mercury jet	7
3.1.2	Proton beam	9
3.1.3	Solenoid	11
3.1.4	Optical diagnostics	11
3.1.5	Cryogenics	12
3.1.6	Current transformer	12
3.2	Simulations of particle flux	13
3.3	MERIT participants	13
4	Particle detectors	15
4.1	General detector requirements	15
4.2	Detector positions	15
4.3	Aluminum Cathode Electron Multiplier	16
4.4	Polycrystalline Chemical Vapour Deposition Diamond	18
4.4.1	Signal generation	19
4.4.2	Diamond readout	20
4.4.3	Charge collection distance	21
4.4.4	Diamond calibration with α -source	23
4.4.5	Extraction of diamond characteristics	25
4.4.6	Simulation of pCVD signal	27
5	Performance test of detectors	35
5.1	pCVD in high intensity proton beam	35
5.2	ACEM in dipole magnet	35
5.2.1	Setup	35
5.2.2	Results	37

6	Experimental setup	41
6.1	Specifications	42
6.1.1	Oscilloscopes	42
6.1.2	Pulse generator - HP81110A	43
6.1.3	Power supplies - CAEN N470	43
6.1.4	Attenuators	43
6.1.5	Cables	44
6.2	Equipment interface	45
6.2.1	Instrument communication	45
6.2.2	LabView interface	46
7	FLUKA simulations	49
7.1	Geometrical model	49
7.2	Simulation objectives	50
7.3	Results	52
7.3.1	Flux of charged particles, MARS and FLUKA	52
7.3.2	Proton beam bending	52
7.3.3	Asymmetry	53
8	Results and observations from the MERIT run	57
8.1	Experimental run	57
8.2	Data analysis	58
8.2.1	Linear offset	58
8.2.2	Bunch integration	58
8.3	Bunch resolution	59
8.4	Equipment scan using particle detectors	59
8.5	Linearity	61
8.6	Target in and out ratio	65
8.7	Probe-pump ratio	67
8.8	Diamond detector in beam line	69
9	Conclusions	71
9.1	Outlook	71
	Bibliography	73
A	Neutrino physics	75
A.1	History	75
A.2	Neutrino oscillations	76

List of Acronyms

ACEM	Aluminum Cathode Electron Multiplier
ALICE	A Large Ion Collider Experiment
ATLAS	A Toroidal LHC ApparatuS
BNL	Brookhaven National Laboratory
CCD	Charge Collection Distance
CERN	Organisation Européenne pour la recherche nucléaire (European Organization for Nuclear Research)
CMS	Compact Muon Solenoid
FLUKA	FLUktuierende KAskade
HV	High Voltage
HWFM	Half Width of Full Maximum
ISOLDE	Isotope Separator OnLine DEvice
LHC	Large Hadron Collider
MERIT	MERcury Intense Target
MIP	Minimum Ionizing Particle
MIT	Massachusetts Institute of Technology
ORNL	Oak Ridge National Laboratory
pCVD	Polycrystalline Chemical Vapour Deposition
PS	Proton Synchrotron
RAL	Rutherford Appleton Laboratory
SPS	Super Proton Synchrotron

List of symbols

α	Alpha particle (Helium nucleus)	
e	Electron	
μ (1)	Charge carrier mobility	[m ² /Vs]
μ (2)	Muon	
ν (1)	Drift speed for charge carriers	[m/s]
ν (2)	Neutrino	
q_e	Elementary charge	[1.602 × 10 ⁻¹⁹ C]
TP	10 ¹² protons	

Chapter 1

Introduction

1.1 CERN

CERN is the world's largest particle physics laboratory, an international organization situated on the Swiss/French border close to Geneva. It currently employs almost 3000 people, including physicists, technicians, engineers and administrators. In addition, some 6500 scientists - half of the world's particle physicists - are visiting CERN.

CERN was founded in 1954 by a total of 12 member states. Since then, the number has grown to 20, plus 8 other countries or organizations with "observer status". The original objective was to study the atomic nucleus, but very soon the work went beyond this, into higher and higher energy regions, using particle accelerators in a continuous seek of the elementary constituents of matter.

Using various kinds of accelerators, CERN is able to accelerate charged particles up to extremely high energies whereupon they collide with either a relatively large, usually non-moving, target or other charged particles going the opposite direction. The latter will be the case for the famous LHC, due to start up in 2008. This is the world's largest accelerator: 27 km long, circular and buried 50 to 150 m below ground. Two proton (or ion) beams will travel in opposite directions in separate pipes, guided by powerful magnets; every single proton reaching energies of astonishing 7 TeV and one beam possessing a total energy of over 360 MJ at collision. Along the accelerator, four main experiments will take place: ALICE, ATLAS, CMS and LHCb, all using different approaches in the study of particles and the secondary particles created in the collisions, allowing the scientists to experimentally test the Standard Model - an attempt to describe fundamental particles and their ways of interacting. For instance, the ATLAS experiment may turn up to find the only particle not observed in - but predicted by - the Standard Model: the Higgs boson, a particle that can shed some light on what "mass" is. On the other hand, should it not be found, theoretical physicists will have a lot of work and rethinking to do. "That would be a lot more interesting", as Chen Ning Yang, Nobel Prize winner and one of the minds behind the celebrated "Yang-Mills Theories", replied when asked to comment about this quest during a seminar given

at CERN.

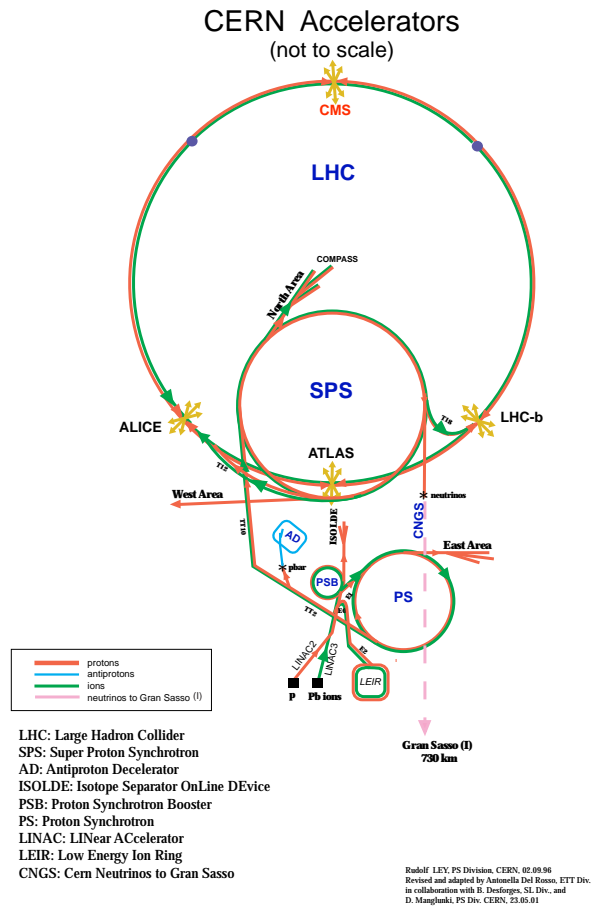


Figure 1.1. CERN accelerator complex.

Apart from having earned the title “where the web was born”, many scientific breakthroughs have occurred at CERN. In 1983 came the first experimental verification of the existence of the W and Z boson by colliding protons and antiprotons in the SPS. The following year (a remarkably short waiting period), the project leader Carlo Rubbia was awarded the Nobel Prize along with his colleague Simon van der Meer for this discovery.

Finally, some clarification about the acronym CERN is probably necessary. Its original meaning was *Conseil Européen pour la Recherche Nucléaire*, a provisional council established 1952. At the founding, the name was changed to *Organisation Européenne pour la Recherche Nucléaire*. Instead of changing to the not as easily pronounced acronym OERN, the name CERN was kept (perhaps thanks to

Richard Feynman, who, so the story goes, suggested: “But the *acronym* can still be CERN even if the name is ...”).

1.2 MERIT

MERIT is short for MERcury Intense Target - a proof-of-principle test for a neutrino factory target taking place at CERN.

The basic concept for this factory is to let a proton beam interact with a free jet of liquid mercury. As the proton beam smashes into the mercury target, secondary particles are created, of which pions and kaons are the major neutrino contributors (kaons mainly decay to a muon and a neutrino or pions). To collect the charged pions from the target vicinity, the entire interaction region is surrounded by a solenoid providing a magnetic field of up to 15 T.

The muons created from the pion decay can be guided into a storage ring where the final step in the decay chain occur:

$$\begin{aligned}\mu^- &\rightarrow e^- + \bar{\nu}_e + \nu_\mu \\ \mu^+ &\rightarrow e^+ + \nu_e + \bar{\nu}_\mu\end{aligned}\tag{1.1}$$

One measure of success for this type of factory is the yield of neutrinos per input proton. To maximize this one must in each step of the decay chain collect and store as many pions and muons as possible. The pions are partly taken care of by mentioned solenoid. As the time for each individual decay is stochastic one typically guides the muons into a storage ring before the final step occur. This storage ring can have the shape of two long, straight sections connected by two smaller semicircles (equipped with bending magnets). Here the muons circulate until decaying and the Lorentz-boost will make the resulting neutrinos continue in a direction practically parallel to one of the two straight sections, since the probability of decaying in the semicircles is low. A neutrino detector is positioned somewhere downstream of one of the straight sections (or both).

Doubtless, the importance of choice of target can not be overrated. At the MERIT experiment it will face the challenge of withstanding 24 GeV/c protons arriving in pulses of 30 TP while a steady, predictable flow of secondary particles is desired. Conventional non-moving solid targets wear out with time as they are constantly bombarded at the same spot, suffering radiation damages and changes in material properties. The novelty of the MERIT target is that it uses a circulating, liquid target since the region exposed to the proton beam is then constantly replaced. Each proton pulse will see a fresh target, which is the main reason why liquid mercury, although toxic and difficult to handle, has been chosen as target material.

Chapter 2

Problem definition

The objective of this thesis is to set up a particle detection system for measurement of the secondary particle flux during the MERIT experiment. This includes:

- Choosing a suitable type of detector
- Learning and handling all the peripheral equipment necessary to power and read out the detectors
- Making simulations of the particle flux in order to confirm previous simulations and estimate the performance required of the system
- Developing a software interface to the data acquisition and detector controlling systems for remote controlling
- Participate in the initial analysis of experimental observations

Chapter 3

MERIT description

The MERIT experiment aims at demonstrating the feasibility of a liquid mercury jet target system and a 15 T pion collecting solenoid, for use in a neutrino factory or muon collider[2]. The behavior of the mercury jet subjected to a proton beam will be studied, with focus on maximum repeatability rate, disruption threshold conditions, magnetohydrodynamic pressure effects and recovery time.

3.1 Experimental setup

3.1.1 Mercury jet

As hinted in the introduction, there are many aspects to consider when choosing a suitable target for a neutrino factory. A plausible scenario for future factories of this kind will be a 50 Hz operation with a beam power of 4 MW - roughly the electrical consumption of 10 000 apartments. At beam-mercury impact, vast amounts of energy are deposited in the target in form of heat (which causes melting or vaporization), pressure waves or triggered nuclear reactions. A solid target exposed to this quickly wears out¹ if it is stationary with respect to the proton beam. Although it is possible to repeatedly replace the target as it degenerates, it is not a satisfying solution, as it would require complicated mechanical assemblies, rather risky for a high radiation environment. It would also put all activities connected to the secondary particle beam on hold during the switch. Furthermore, as the target has been exposed to a high intensity beam, it has become “hot”, i.e. radioactive, which requires special handling. Ideally, once you have started up your neutrino factory, you do not want anything to enter the area more than necessary.

Rotating-wheel targets have been used for a beam power less than 1 MW, but for a quadrupling of the power not even this trick is satisfying[2]. Having dismissed the solid state phase of a target the natural choice would be a liquid one. But water, for example, would not do since the hydrogen and oxygen nuclei are too light (a low-Z nucleus yields relatively few secondary particles when interacting

¹A carbon target would have a lifetime of one or two days due to sublimation[2].

with a proton beam). Higher up in the periodic table we find mercury, which has the great advantage of being liquid at room temperature, although i.e. molten lead has been considered as a target candidate. This feature is important enough to justify the complicated handling required for this toxic liquid.

When choosing a liquid as target, one faces another question: either to confine the liquid inside a pipe, or let the proton beam impact directly on a free jet. Again, the induced pressure waves might seriously damage the pipe by pitting, why in MERIT the target is free mercury.

The very point about using a liquid is its fluidity. The mercury will obviously suffer from all of the mentioned stresses. But if the liquid is a moving jet with high enough velocity, the volume element exposed to one proton pulse (i.e. a heated up and dispersed region) will move forward until the next proton bunch arrives. So the next time the beam hits the mercury, it will enter a smooth target, unaffected (if tuned correctly) by previous pulses.

In MERIT, the mercury target is manifested as a jet, with a cross section of about 1 cm^2 and a maximum velocity of 15 m/s [2].

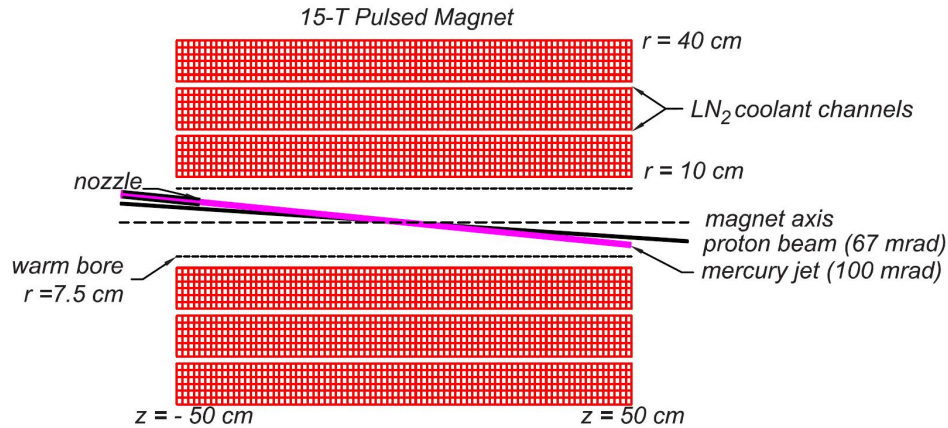


Figure 3.1. Schematic sketch of mercury jet and proton beam surrounded by a solenoid.

The high speed serves to make the interaction region (the overlapping between mercury and proton beam) as rod-like as possible by reducing the curvature - due to gravitational forces on the mercury - of the jet, but also - even more important - to ensure that a large enough, by the proton beam unperturbed, region has enough time to replace the mercury just hit by the beam. So what happens to the mercury, on a macroscopic level, at beam impact? Most importantly, the mercury jet is soon dispersed and the smooth surface completely disrupted (see fig 3.2).

Clearly, this deformed shape is highly undesired when striving for a predictable flow of secondary particles from the target: a disrupted jet would yield less particles, having less effective target volume as seen from the proton beam. The rapid energy deposition inside the mercury preceding the visible disruption induces expanding cavitation bubbles inside the target. This effect is not as visually

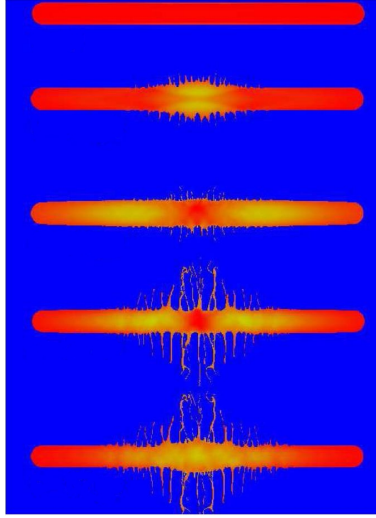


Figure 3.2. FronTier simulation from 0 to 67 μs of a 1-cm-diameter mercury jet in zero magnetic field subject to instantaneous energy deposition with a Gaussian spatial profile peaked at 100 J/gm[4].

dramatic as the later jet disruption but nevertheless a potential problem for the same reasons. These obstacles are partly overcome by a high jet velocity, but a major supporter in keeping the jet shape smooth is the magnetic field provided by the solenoid surrounding the interaction region by performing a magnetic pressure on the target (see 3.1.3).

As seen in fig 3.1, there is a relative angle between the jet and the proton beam of 33 mrad. A qualitative explanation is this: with no relative angle, the overlapping region between jet and beam would be very long (infinite if not for gravity). With an infinitely long target, all incoming protons would interact with it, but the forward-directed secondary particles would at some point be reabsorbed by the mercury, thus reducing the total yield. On the other hand, a very thin target would not produce many secondary particles in the first place. In other words; different angles correspond to different effective target lengths. The angle corresponding to two interaction lengths² seems to be the optimal one[2].

3.1.2 Proton beam

A future neutrino factory of this kind is ment to function at up to 50 Hz, meaning the mercury target will be hit by a proton pulse every 20 ms. The protons provided by the PS accelerator at CERN have a momentum of either 24 GeV/c or 14 GeV/c³ and are extracted into the TT2 tunnel (see fig 1.1) where the experiment will take

²One interaction length is defined as the target length required for reducing the initial proton beam intensity a factor e^{-1} .

³The maximum pump-probe time separation is longer at the lower momentum.

place. However, in this proof-of-principle experiment, a continuous 50 Hz operation (which would be equivalent to a 4 MW proton beam) is not possible due to the time required to reload the accelerator after each PS extraction and limitations in magnet cooling⁴. To get around this, the protons in the PS ring are extracted in two groups called “pump” and “probe”.

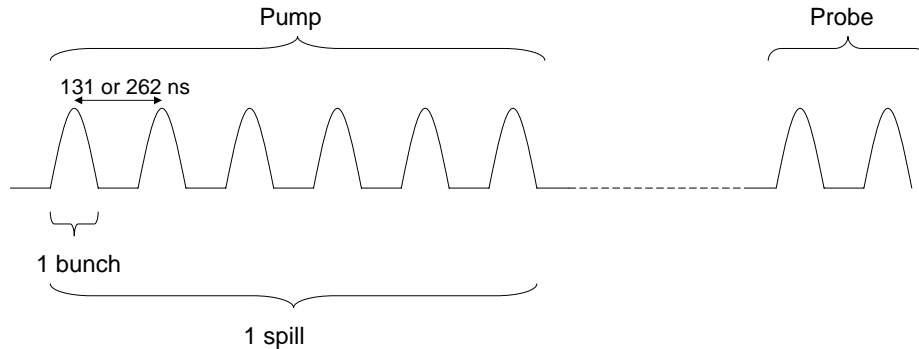


Figure 3.3. The pump-probe concept. The time between the pump and the probe pulse will be varied from μs to ms. At most, there can be 16 micro-bunches in total.

The time separation within each group is either 131 ns or 262 ns⁵, while the separation between the pump and probe is adjustable from some hundreds of nanoseconds to one milliseconds. The pump hitting the mercury target triggers dispersion of the jet shape and induces cavitation bubbles if the intensity is high enough. However, it takes some time before these effects become visible; tens of microseconds is estimated for the dispersion. As the time from the first to the last bunch in the pump group is about 1-2 μs , the mercury response to each of these bunches is expected to be fairly constant. The purpose of the next spill - the probe - is to investigate the behavior of the target. Starting from a relatively short pump-probe time separation, one can indirectly measure how the disruption of the target proceeds by looking at the intensity of secondary particles. Initially, the disruption and cavitation increase, rendering less secondary particles from the probe impact. But after some time, the target starts to recover again as the mercury jet travels forward, replacing the disrupted mercury with unperturbed. By increasing the pump-probe time further, the time at which this phenomenon occur can in principle be determined by scanning a wide range of pump-probe times and investigate at what time the detectors’ responses to the probe spills are the same as for the pump spills. For a 50 Hz operation, this time must be strictly shorter than 20 ms, during which the mercury has covered about 40 cm.

⁴Furthermore, the PS machine is usually providing beam for several different users during a 16 second cycle. To gain exclusive right of all the beam is barely possible.

⁵The PS can be operated in “Harmonic 8” or “Harmonic 16”. In Harmonic 8 mode, the PS is filled with eight equidistant proton buckets and the time between each bucket is 262 ns. At Harmonic 16, the number of buckets are doubled and the time separation halved.

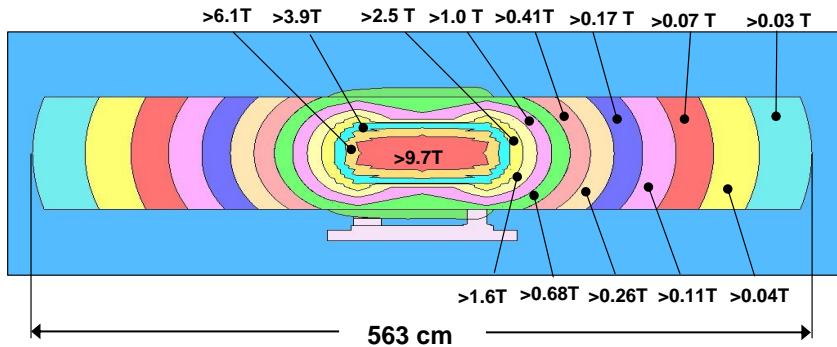


Figure 3.4. Stray field from the solenoid at 10 Tesla.

3.1.3 Solenoid

Surrounding the interaction region is a solenoid capable of generating a magnetic field of up to 15 Tesla. The coil is divided into three segments that are cooled with liquid nitrogen. The magnet works in pulsed mode where a short current pulse of 7200 A generates the desired magnetic field. To do this, the bulk temperature of the magnet must be lowered to 85 K. When this temperature is reached, a voltage can be applied over the coils and a current flows through the magnet, generating a magnetic field inside. Since the inductance of the solenoid is high, almost 0.5 Henry, it takes several seconds for the current to reach a level where the induced axial magnetic field is high enough. During this time the magnet temperature increases from 85 K to 115 K. When the magnetic field peaks, a liquid jet of mercury is squirted from a nozzle into the center of the solenoid where it interacts with a proton beam.

The magnetic field confines most of the charged secondary particles from this interaction to the center of the solenoid and its main purpose is to collect the charged pions. A less obvious effect is that on the mercury jet. As the proton beam enters the mercury jet, the rapid energy deposition will cause its shape to be heavily deformed and then dispersed. If the goal is to have a neutrino factory with a predictable and stable yield of secondaries, this is not good. Now, although the mercury itself is not magnetic the magnetic field still performs a magnetohydrodynamic pressure on the fluid, which serves to stabilize the surface as seen in figure 3.5.

3.1.4 Optical diagnostics

To study the behavior of the mercury jet four high speed cameras are positioned along its trajectory. As the radiation levels are quite high this close to the target, conventional cameras can not be used⁶. Instead, the mercury jet is illuminated

⁶A web camera was installed in the tunnel one meter away from the solenoid to monitor the equipment during the installation phase. At the first target-in extraction it stopped working.

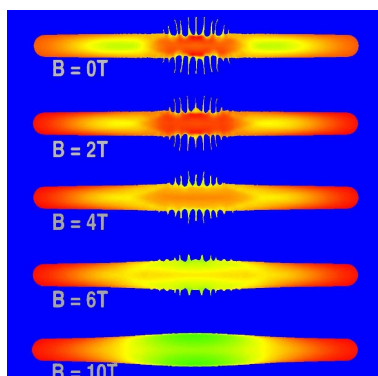


Figure 3.5. Simulation of mercury jet $50 \mu\text{s}$ after energy deposition in a magnetic field ranging from 0 to 10 Tesla parallel to the jet axis[4].

with a laser from one side. The light is reflected in a mirror at the other side and guided into optical fibers which transfer the signal to a digital frame grabber in the access tunnel. The maximum sampling rate of these side-view cameras is 2000 frames per second and they will provide a direct measurement of the jet quality and mercury disruption development.

3.1.5 Cryogenics

The magnet works in pulsed mode which includes a ramping up of the current, a flat top with constant magnetic field and a ramp down. The whole sequence takes about 15 seconds and during the flat top, there is over 7000 Amperes flowing through the magnet coils. Although the total resistance of the solenoid is low, this will significantly heat up the whole device. And when the temperature goes up, the resistance follows and another 15 T pulse would increase the temperature even more. After a few cycles the target system and optical diagnostics inside the solenoid would be at risk. To avoid this, the solenoid is cooled with liquid nitrogen to 85 K. At this temperature, one single 15 Tesla pulse increases the temperature of the solenoid some 30 K. The time required to recool the magnet is about 45 minutes, setting a lower limit of the repeatability rate.

3.1.6 Current transformer

A few meters upstream of the solenoid is a current transformer. Its purpose is to give detailed information on the proton bunch structure just before target impact. The positively charged beam is passing coaxially through the stout ring seen in figure 3.6 whereupon a current is induced in a circuit. This mirror current is digitized at 500 MHz and by integrating the signal one can calculate the intensity for each bunch.



Figure 3.6. The TT2a current transformer.

3.2 Simulations of particle flux

Simulations have been made of the flux of secondary particles from the proton-mercury interaction. Displayed in figure 3.7 is the flux of charged hadrons which is of major interest from a detector point of view (see chapter 4).

The effect of the multi-tesla magnetic field inside the solenoid is clearly visible. The trajectory for a charged particle will be a helix resulting in a forward shifted total flux of charged secondaries. It will also result in more particles making it out from the solenoid bore without being absorbed in the coils. The results from these simulations will be taken into account when deciding where to place the particle detectors. One should also have in mind that in the simulations, the incoming protons are considered an instantaneous event, while in reality they are spread out over some 40 ns.

3.3 MERIT participants

BNL, Princeton - project oversight, nozzle development, beam window design, optical diagnostics

CERN - Proton beam facility interfaces, secondary flux detectors

MIT - Magnet design fabrication

ORNL - Hg target system design fabrication

RAL - Magnet cryogenics

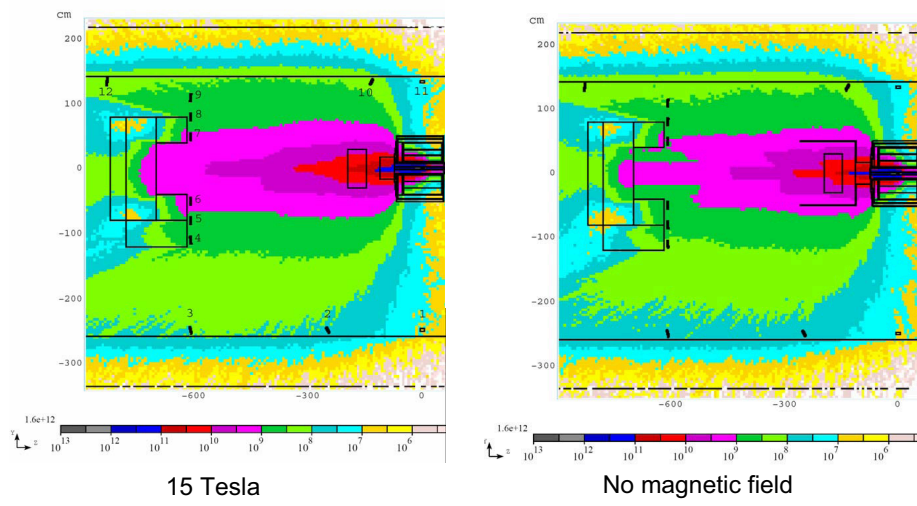


Figure 3.7. Flux of secondary particles (charged hadrons per cm²) with different magnetic fields. Total number of protons on target is $3 \cdot 10^{13}$ [13].

Chapter 4

Particle detectors

4.1 General detector requirements

There are three major things to consider when choosing a detector type for MERIT. First of all, the time-scale is short. Individual proton bunches are separated from only 131 ns and the width of each bunch is roughly 40 ns. The rise and fall time of the signal from a detector must be in the order of nanoseconds to give a good pulse resolution and catch the sudden changes in particle fluxes, as expected from mentioned simulations.

Another issue is the very high intensity: up to $\sim 10^7$ charged particles per cm^2 per nanosecond several meters away from the solenoid[13]. Many conventional detectors are designed to detect only single or a few particles, e.g. beam loss monitors. If used in MERIT, a detector of this kind would immediately be destroyed or saturated.

Finally, the magnetic field from the solenoid is still quite strong even at a distance of a few meters. A reasonable requirement would be that a detector must be virtually unaffected by magnetic fields up to some 400 G.

4.2 Detector positions

The main objective for the particle detectors is to make a signal-per-proton comparison for the pump and the probe. In this sense, the positioning of the detectors is not crucial; it would suffice to give them a clear view of the solenoid and make sure the flux is neither too high nor too low. On the other hand, it would be a waste not to seize the opportunity to try to see some other things apart from possible pump-probe variations.

One interesting thing would be to measure asymmetries in the angular distribution of the particle flux. This could indicate that the beam is not centered on the target, hence biasing the net production of secondaries in one direction or the other. It could also indicate that it is the target that is displaced from its nominal position. By placing detectors in pairs with identical angles to the target

one can compare the amplitudes of the signals. For this purpose, we have two detector positions on the beam dump with the same angle and distance to the target and another pair at 20° from the target positioned at the left and right wall (see figure 4.1). There is also a detector position right in the beam line, but behind the dump. While the other detectors should give more signal when the beam interacts with a lot of mercury inside the solenoid, the ones placed here should do the opposite as less of the beam reaches the dump - an effect that can be useful when cross checking the data.

Three types of detectors have been considered: ACEMs, PIN-diodes and diamond detectors.

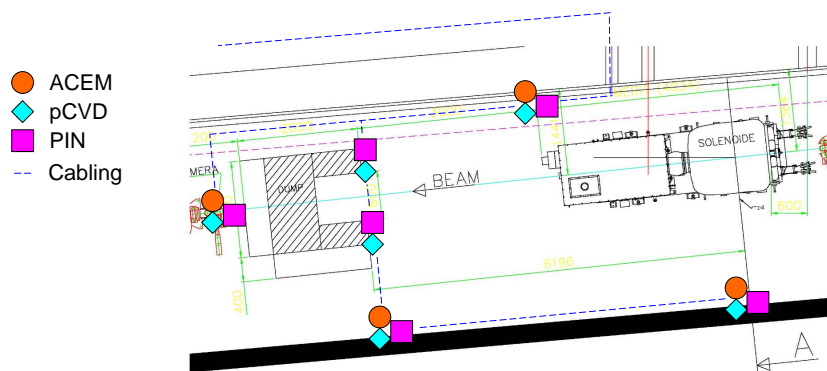


Figure 4.1. Detector positions and cabling (detector voltage and signal).

4.3 Aluminum Cathode Electron Multiplier

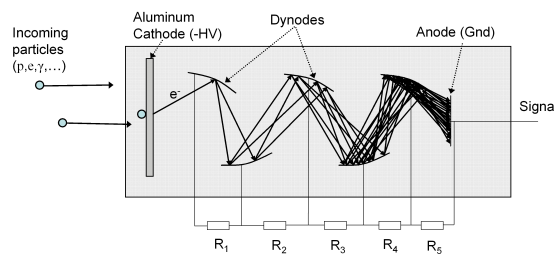


Figure 4.2. Schematic of the ACEM detectors.

The ACEM detector operates in principle as a regular photomultiplier, but with an aluminum foil as cathode. As the foil is irradiated by incoming particles (charged and photons), secondary electrons are knocked out. Between the anode

and cathode is a series of dynodes; secondary emission-electrodes. The dynodes are connected to a voltage divider, yielding a potential difference between each dynode. The electric field between them accelerates the emitted electrons from one dynode to the next where even more electrons are emitted, given enough energy. With N dynodes, the total gain, M , is:

$$M = \prod_{i=1}^N g_i \quad (4.1)$$

where g_i is the gain at dynode i and M the final number of electrons produced from one cathode-emitted electron collected at the anode, where a signal is induced in the circuit.

Dynodes	10
Cathode surface area	7 cm ²
Max current	20 mA (short pulses)
Max HV	1.5 kV

Table 4.1. Some ACEM characteristics

Typical rise and fall times are in the order of nanoseconds. In “ordinary” circumstances, where the flux of incoming particles is low (single particle resolution), typical voltage bias is about 1 kV. However, in MERIT the flux may be as high as 10^7 charged particles per nanosecond. To protect the detector from saturation and high currents, the value of M will have to be low, which is realized by applying a low voltage. Hence, the cathode-emitted electrons will not be as much multiplied as guided between the dynodes toward the anode. It is unclear if this detector type will behave normally at such a low operating voltage, so another system is necessary for which the ACEMs can serve as a back up.

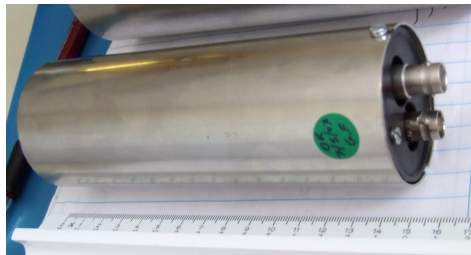


Figure 4.3. One ACEM detector.

The ACEM detector is basically just a tube with one voltage input and a signal output. It is covered with a 1 mm thick layer of μ -metal on the sides and the top that provides shielding from light and external magnetic fields that could disturb the electron paths between the dynodes.

4.4 Polycrystalline Chemical Vapour Deposition Diamond

Charged particles traversing matter mainly lose their energy by ionization processes, creating electron-hole pairs (e-h pairs) along their paths¹. This property can be utilized in a detector by applying an electric field across the detector body, separating and accelerating the e-h pairs toward the contact surfaces. This movement of charge inside the detector generates a current in the circuit which can be displayed and recorded on a suitable device.

Property	Value	Symbol
Density	3.52 g/cm ³	ρ
Electron mobility	0.22 m ² /Vs	ν_e
Hole mobility	0.16 m ² /Vs	ν_h
Electron saturated velocity	$2.3 \cdot 10^5$ m/s	$\nu_{s,e}$
Hole saturated velocity	$1.0 \cdot 10^5$ m/s	$\nu_{s,h}$
Bandgap	5.45 eV	-
Energy to create one e-h pair	13 eV	E_{eh}
Average ionization density for a MIP (e-h pairs/ μ m)	36	ρ_{ion}

Table 4.2. Typical diamond characteristics[7].

Two types of solid state detectors have been considered for this experiment; silicon diodes² and diamond detectors. They are similar in terms of functionality and generated current per detected charged particle. Both are also considered fast detectors, with rise and fall times of a few nanoseconds. Two things, however, are in favor of the diamond version, both concerning the high intensity of secondary particles in MERIT. First, the diamond detectors are more radiation hard than silicon. They have been verified to withstand fluxes of 10^{15} protons without any significant deterioration[7]. Second, a MIP generates more e-h pairs per μ m in silicon than in a diamond (and thus a higher integrated current)[3]. This is a good property when detecting single particles, but a potential drawback for MERIT. The charge generated in the detectors must be extracted between two proton bunches (131 or 262 ns) in order to clearly identify which part of the signal comes from which bunch. Using a typical detector with an area of 1 cm², the order of magnitude for these currents is several amperes for a diamond³ - even higher for a PIN diode - given that it is possible to drain the detector of free charge carriers completely between two bunches. It is not entirely clear that a PIN diode can survive such a current. The choice thus fell on diamond detectors as the main

¹One particle with sufficient energy to create any e-h pairs is called a MIP - Minimum Ionizing Particle.

²PIN-diodes, consisting of two p- and n-doped layers with a pure intrinsic layer in between.

³Rough estimation: With a detector thickness of 500 μ m, 10^8 MIPs yields $10^8 \cdot 36 \cdot 500 = 1.8 \cdot 10^{12}$ e-h pairs. Draining the diamond of this amount of charge in 50 ns would be equivalent to a current of $\frac{\Delta Q}{\Delta t} \approx 6$ A

detector type since these have been tested satisfactory in conditions similar to that of a secondary particle detector position in MERIT, when a piece of diamond were subjected to 10^9 protons distributed over eight bunches while giving a reliable signal[7].

The diamonds are grown with a chemical vapor deposition technique which gives a very pure sample. The finished detectors have a size of $0.5 \times 7.5 \times 7.5 \text{ mm}^3$. The top and bottom are coated with a conducting Cr-Au layer for signal read-out.

4.4.1 Signal generation

A voltage U applied to the two diamond contact surfaces yields an internal electric field $E = \frac{U}{d}$, d being the distance between the contacts. The field accelerates internal free charge carriers toward the anode or the cathode, depending on charge polarity, which causes a change of potential on the electrodes and a current is induced in the circuit[7]:

$$I_e = n_e \frac{q_e \nu_e}{d} \quad (4.2)$$

where subscript e denotes electrons as charge carrier (h for holes). n_e is the number of free electrons and ν_e the drift speed for electrons. For moderate voltages this is proportional to the applied voltage[7]:

$$\nu_e = \mu_e E = \mu_e \frac{U_d}{d} \quad (4.3)$$

where U_d is the voltage over the diamond. This relationship breaks down for high voltages as the drift velocity approaches the saturation velocity, ν_s . At these levels the expression:

$$\nu_e = \frac{\mu_e E}{1 + \frac{\mu_e E}{\nu_{s,e}}} \quad (4.4)$$

is a better approximation[10]. Typical operating voltage is 500 Volts and is within the region where the drift speeds are close to saturated.

The drift time for an electron is limited by the distance from its starting point. Treating the diamond as an ideal capacitor, the electron yields a constant current while between the contact surfaces. The collected charge for an electron released at a distance z from the anode is given by:

$$Q_c = \int_0^t I_e(t) dt \quad (4.5)$$

where t is the time for the electron to reach the anode. For an ideal diamond crystal, the lifetime of an electron is infinite, but in reality impurities and the boundaries of the polycrystalline structure cause drifting charges to be trapped and reabsorbed. This is a statistical process and one can assign each type of charge carrier a lifetime τ to model this loss of charge. The collected charge for a group

of n_0 electrons starting at z will be:

$$Q_c = q_e \int_0^{\frac{z}{\nu_e}} n_0 e^{-\frac{t}{\tau_e}} \frac{\nu_e}{d} dt = \frac{n_0 q_e \nu_e \tau_e}{d} \left(1 - e^{-\frac{z}{\nu_e \tau_e}}\right) \approx n_0 q_e \frac{z}{d} \quad (4.6)$$

The last expression is only valid when the lifetime is very long compared to the drift time required for an electron to reach the anode (z/ν_e). A MIP will liberate electrons (and holes) throughout the whole diamond. Thus, for the electrons starting off close to the cathode, the collected charge is close to the original number of cathode-close electrons (given that the lifetime is long compared to the required drift time for an electron to traverse the diamond), while, somewhat counter-intuitively, those created at the anode-side will barely make any contribution at all to the total collected charge.

Assuming that one MIP generates n electron-hole pairs, equally spaced throughout the diamond, the collected charge due to the moving electrons can be considered a sum of each individual electron-hole pair contribution with different starting positions, $z_i = \frac{i}{n}d$. Consider the collected charge from the electron contribution:

$$Q_{c,e} = \sum_{i=1}^n q_e \frac{\nu_e \tau_e}{d} \left(1 - e^{-\frac{z_i}{\nu_e \tau_e}}\right); \quad z_i = \frac{i}{n}d \quad (4.7)$$

Again, treating the lifetime as long compared to the drift time, a first order Maclaurin series gives:

$$Q_{c,e} = q_e \frac{\nu_e \tau_e}{d} \sum_i \left(\frac{i}{n} \cdot \frac{d}{\nu_e \tau_e}\right) = \dots = q_e \frac{n+1}{2} \approx q_e \frac{n}{2}; \quad n \text{ large} \quad (4.8)$$

Hence, even for a perfect diamond with infinite lifetime, the collected charge from a MIP with high enough kinetic energy to cross the entire diamond is only half the one generated (since one e-h pair represents two elementary charges).

4.4.2 Diamond readout

A few remarks on the design of the readout circuit should be made (see figure 4.4).

As mentioned, the expected currents are of the order of several amperes. But this is only possible if the bias voltage across the diamond is maintained during the entire proton bunch sequence. Should the voltage drop, the current will do likewise. Therefore, it is of great importance that the electric potential at the contact surfaces is stable. This is the purpose of the large 100 nF capacitor in the circuit, serving as a charge reservoir. The power supply alone can not maintain the operating voltage while draining the diamond of such a large current, as the maximum deliverable current of such a device is usually limited to some mA. When the diamond is not exposed to any radiation, the leakage current under 500 V is less than one nA. This means its resistance is in the order of TΩ. In equilibrium virtually all the voltage will be over the diamond and the capacitor, with a minute current from the power supply flowing through the circuit. The

protection resistor of 1 k Ω in series with the power supply is to avoid short circuit. Below the diamond is another resistor of 1 M Ω over which the output is taken (50 Ω cable and an oscilloscope with the same input impedance).

As the diamond detector is exposed to ionizing radiation, it can be considered to experience a dramatic decrease in resistance due to its internal free charge carriers (it becomes quasi-conducting). The capacitor, that has been charged up at 500 V, serves as a voltage source that causes a current to flow through the circuit. While not irradiated, the leakage current was fully compensated by the current from the power supply, but now this milliampere current is too low to keep the diamond at 500 V. Instead, this has to be done by the capacitor. To do this for 8 consecutive proton bunches, the total charge drained from the diamond must be significantly lower than the charge stored in the capacitor. The number of e-h pairs created is:

$$Q_d = 8 \text{ bunches} \cdot 36 \text{ e-h pairs}/\mu\text{m} \cdot 500 \mu\text{m} \cdot 10^8 \text{ MIPs} \cdot q_e = 1.4 \cdot 10^{13} q_e$$

while the initial charge stored in the capacitor is:

$$Q_c = U_c C = 500 \text{ V} \cdot 100 \text{ nF} = 3.1 \cdot 10^{14} q_e \approx 22Q_d^4 \quad (4.9)$$

So, the maximum collectible charge from the diamond is less than 5 percent of that stored in the capacitor. Hence, the capacitor should be able to maintain the voltage across the diamond with a total voltage drop less than a few percent.

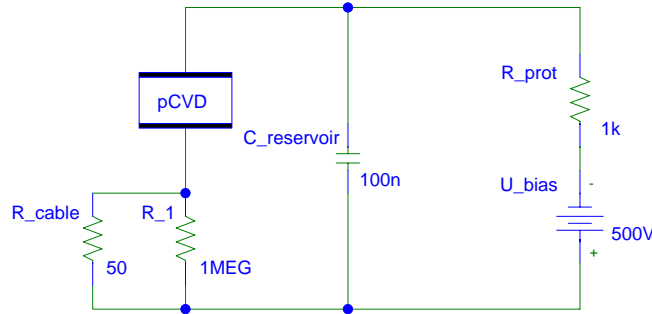


Figure 4.4. Diamond readout circuit.

4.4.3 Charge collection distance

The charge collection distance (CCD) is a parameter closely coupled to the charge carrier lifetime and can be interpreted as the average distance that an electron-hole pair move apart. In the ideal case, this distance is equal to the diamond thickness, meaning that all the electrons and holes are collected at the electrodes. Finite

⁴Subscript *c* and *d* denotes capacitor and diamond.

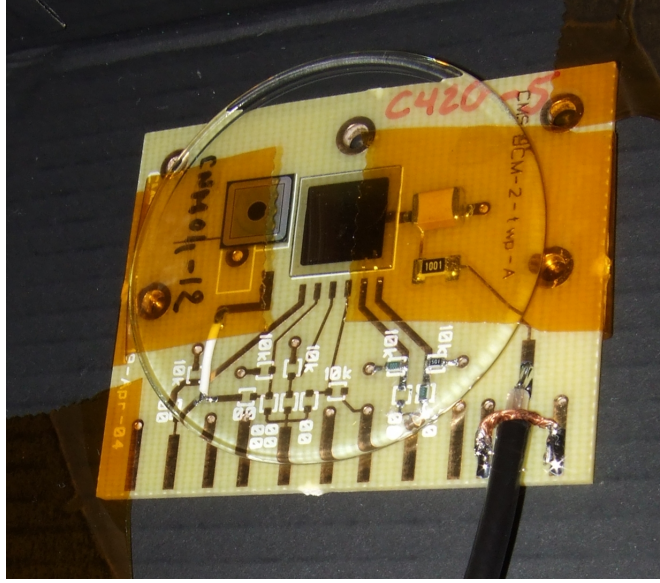


Figure 4.5. Circuit board. Diamond with a 7.5×7.5 mm Au-Cr contact surface in the middle. To the left of this a PIN-diode for calibration purpose. The two detectors are covered by a protective concave glass disc.

lifetimes limits this number to, at present, about half the diamond thickness for polycrystalline samples. Definition of the CCD:

$$\delta = \frac{\int I_{tot}(t) dt}{\rho_{ion} q_e} = \frac{Q_{c,e} + Q_{c,h}}{\rho_{ion} q_e} \quad (4.10)$$

where ρ_{ion} is the linear ionization density for a MIP traversing the detector. To measure this parameter, the detector was exposed to a suitable radiation source (a β -source in this case, ^{90}Sr). By integrating the induced current from a single MIP, one gets $Q_{c,tot}$. For illustrative purposes one can make the assumption that the number of collected electrons (here denoted as a fraction λ of the originally generated e-h pairs) is equal to that of the holes, yielding:

$$\delta \approx \frac{\lambda_e Q_{g,e} + \lambda_h Q_{g,h}}{\rho_{ion} q_e} = \frac{\lambda_e \rho_{ion} dq_e + \lambda_h \rho_{ion} dq_e}{\rho_{ion} q_e} = (\lambda_e + \lambda_h) d \leq d \quad (4.11)$$

The final step follows from eq 4.8, telling us that neither of the λ :s, in this model, can exceed 1/2. Since the integrated current is due to moving holes as well as electrons, this type of measurement is not feasible if one would like to investigate further the individual properties of these complementary charge carriers. For the diamonds used in MERIT, the collection distance has been measured to about $220 \mu\text{m}$, or $0.44d$.

4.4.4 Diamond calibration with α -source

To determine other parameters for the diamond, the response when exposed to radiation was measured by using ^{241}Am as an α -source. The main difference from β -radiation is that α -particles have a much shorter penetration depth. The setup is described in fig 4.6.

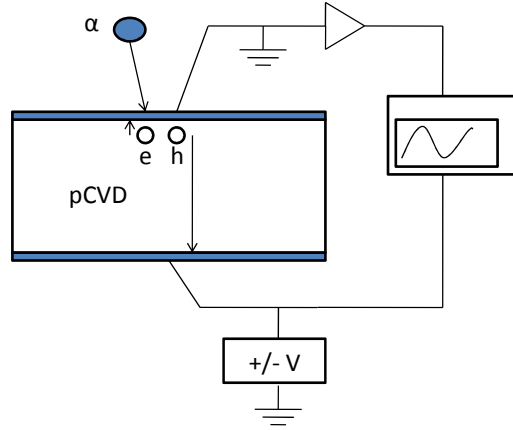


Figure 4.6. Sketch (simplified) of the α -calibration. Electrons will go one way and holes the other, depending on the bias polarity. The signal is amplified and recorded on an oscilloscope.

The kinetic energy, E_0 , of the α -particles is 5.5 MeV. Between the source and the diamond is an air gap of $d_{air} = 0.6$ cm followed by a Au-Cr contact with thickness $d_{Au} = 250$ nm. The stopping power for an α -particle in air is $E'_{air} = 712$ MeV/g/cm² and $E'_{Au} = 233$ MeV/g/cm² in gold (the contact is assumed to be pure gold). Densities for air and gold are $\rho_{air} = 1.2 \times 10^{-3}$ g/cm³ and $\rho_{Au} = 19.3$ g/cm³. Given these numbers, the average energy loss for an α -particle before entering the carbon region in the diamond detector is:

$$E_{loss} = E'_{air}d_{air}\rho_{air} + E'_{Au}d_{Au}\rho_{Au} = 625 \text{ keV} \quad (4.12)$$

As the stopping power in diamond is relatively high, an α -particle will be completely stopped after about 14 μm . Thus, one α -particle deposits $E_0 - E_{loss} = 4.87$ MeV. Assuming that all energy is converted to creation of electron-hole pairs this yields[7] 3.7×10^5 pairs.

Two points about this measurement should be made. First, the polarity of the bias voltage at the side where the α -particles hit is very important as it determines which type of charge carrier will traverse the diamond to the other side. With a negative bias voltage, the top side becomes the anode and the bottom the cathode with electrons and holes drawn to the opposite charge side. As the α -particle penetration depth is very thin compared to the thickness of the diamond (500 μm), almost all the e-h pairs will start off from the top, so the time for the electrons to

reach the anode is much shorter than the time for the holes to reach the cathode. In this case, the integrated charge due to electrons is close to negligible (see eq. 4.6).

In MERIT, the diamond will be exposed to high fluxes of light MIPs, e.g. hadrons, electrons and muons which easily pass $500 \mu\text{m}$ of diamond with an average energy loss of some $500 \text{ eV}/\mu\text{m}$, the creation of electron-hole pairs no longer restricted to the surface regions.

Second, these numbers are only valid for an α -particle whose trajectory is perpendicular to the diamond contact surface. The ones deviating from the shortest path will lose more energy on their way and yield less electron-hole pairs. This effect is taken into account using the histogram feature of the oscilloscope. Each signal with a high enough peak triggers the scope, the signal is recorded and analyzed and the maximum amplitudes are placed in a histogram. The high-voltage end of the histogram gives the expected signal for the most energetic incoming α -particles (e.g. the ones with shortest air distance to travel). See figure 4.7.

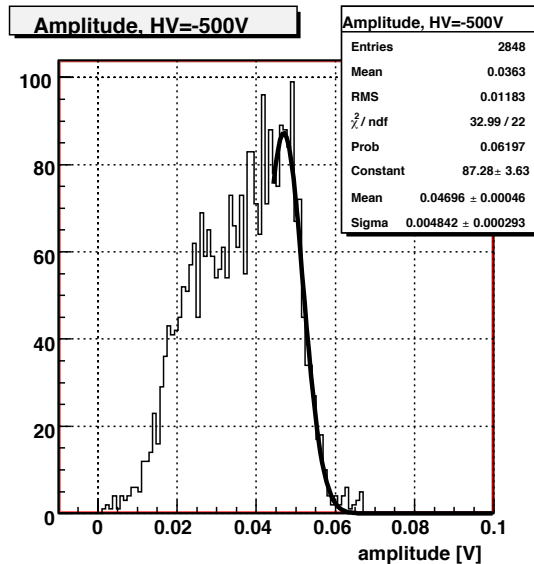


Figure 4.7. Histogram over signal peaks for diamond sample C420-5 exposed to α particles.

The high-end side is here fitted with a gaussian. The voltage peak for the particle trajectories perpendicular to the diamond surface has been interpreted to roughly correspond to the value where the downslope of the histogram is steepest. The results from these measurements are presented in table 4.3.

There are still signals with higher amplitudes than the values presented here. Part of this can be blamed on noise and that the americium sample occasionally emits multiple α -particles, yielding a higher signal than a straight-on single nucleus even if they are separated a few nanoseconds, or have covered a longer distance in air.

Diamond sample	Signal peak	Diamond current
C-420-1	43 mV	2.08 $\mu\text{A}/\text{MeV}$
C-420-2	48 mV	2.32 $\mu\text{A}/\text{MeV}$
C-420-3	50 mV	2.42 $\mu\text{A}/\text{MeV}$
C-420-5	50 mV	2.42 $\mu\text{A}/\text{MeV}$
C-420-6	47 mV	2.27 $\mu\text{A}/\text{MeV}$
C-420-8	36 mV	1.74 $\mu\text{A}/\text{MeV}$

Table 4.3. Results from α -calibration of diamond samples. The numbers in the third column are adjusted for an amplification of 85 and an input impedance of 50 Ω on the oscilloscope.

The width of the signal is roughly 2 ns for the holes. By reversing the polarity and doing the same measurements for the electrons, the signal width is estimated to be 6 ns but with a lower amplitude. Yet, the integrated signal remains more or less unchanged.

4.4.5 Extraction of diamond characteristics

Some vital parameters in making a decent diamond current model can be extracted from the mentioned measurements. Of interest are the charge lifetime (τ), drift velocity (ν) and the carrier mobility (μ) for the two carrier types.

First, we recall that the integrated signals for the holes and electrons with an α -source are roughly equal, or, in other words, the “loss” of charge is about the same regardless of carrier type. Assuming this is also the case when using ^{90}Sr , along with $Q_{c,e} = Q_{c,h}$ and $\delta = 0.44d = 220 \mu\text{m}$, we get from (4.7) and (4.10):

$$2 \times \frac{\nu_h \tau_h}{d \rho_{ion}} \sum_{i=1}^n \left[1 - e^{-\frac{z_i}{\nu_e \tau_e}} \right] = \delta = 0.44d \Leftrightarrow$$

$$\frac{\nu_h \tau_h}{d} \sum_i \left[1 - e^{-\frac{i}{n} \cdot \frac{d}{\nu_h \tau_h}} \right] = 0.22 \rho_{ion} d = 0.22n \quad (4.13)$$

Solving the equation (numerically) gives:

$$\frac{\nu_h \tau_h}{d} = 0.22 \Leftrightarrow \nu_h \tau_h = 1.95 \cdot 10^{-4} \text{ m} \quad (4.14)$$

This applies for the electrons (ν_e, τ_e) as well. The same relation could have been calculated using the α particle response instead, but the signal data from that series (only averaged signals available) are less reliable than the CCD value using ^{90}Sr . However, the α responses can be fruitful in making a rough estimation of the absolute values of ν and τ by modeling the diamond current as an exponential function;

$$I_h(t) = n_0 \frac{\nu_h \tau_h}{d} e^{-t/\tau_h}; \quad \begin{cases} n_0 = \rho_{ion} d \\ t \in [0, \frac{d}{\nu_h}] \end{cases} \quad (4.15)$$

This current is amplified with a factor of 85 (G) into a 50 Ohm impedance. The bandwidth of the amplifier is $f_0 = 500 \text{ MHz}$ and it is modeled with the first order

transfer function[11]:

$$H_{amp}(\omega) = \frac{G}{1 + j\frac{\omega}{w_0}}; \quad w_0 = 2\pi f_0 \quad (4.16)$$

Corresponding impulse response:

$$H_{amp}(t) = G\omega_0 e^{-w_0 t}; \quad t \geq 0 \quad (4.17)$$

Since the analog bandwidth of the oscilloscope (GHz) is much larger than that of the amplifier, it has been neglected here. The signal measured on the oscilloscope is a convolution:

$$U(t) = R \cdot I_h(t) * H_{amp}(t) \quad (4.18)$$

The final step is to adjust ν_h and τ_h so equation (4.14) is satisfied on the one hand, and that the output signal $U(t)$ is fairly similar to the ones in the α measurements - 50 mV peaks and about 2 ns long.

Evidently, there is no perfect fit; the modeled pulse is either too long or too high. The chosen values are:

$$\begin{cases} \nu_h = 1.75 \cdot 10^5 \text{ m/s} \\ \tau_h = 0.9 \text{ ns} \end{cases} \quad (4.19)$$

The main objective for this choice is that it corresponds to the measured voltage peaks of 50 mV, although the modeled signal width is longer than the measured *averaged* signal width. Being an average, this property is given lower credibility since it includes many signals where the α -particle has loosed more energy than the straight-on ones and so have voltage peaks as low as 10-15 mV (see figure 4.7). A signal with this peak amplitude, and a lifetime as short as 0.9 ns, will quickly drown in noise and reduce the average pulse width.

Exploiting that the integrated charge is about the same for electrons at a positive bias voltage, but with about a third in peak amplitude, finding the corresponding electron carrier values is analogous:

$$\begin{cases} \nu_e = 5.83 \cdot 10^4 \text{ m/s} \\ \tau_e = 2.7 \text{ ns} \end{cases} \quad (4.20)$$

One vital property remains to find: the charge carrier mobility μ . With the data available, this is somewhat cumbersome, but one can make a rough estimation. At 500 V, the diamonds operate close to the saturation velocity for the charge carriers (see equation (4.4)). Assuming that $\nu(500 \text{ V}) \approx 0.9\nu_s$ for both electrons and holes, one gets:

$$\mu = \frac{\nu}{E \left(1 - \frac{\nu}{\nu_s}\right)} = \frac{\nu}{0.1E} \Rightarrow \begin{cases} \mu_h = 1.75 \text{ m}^2/\text{Vs} \\ \mu_e = 0.583 \text{ m}^2/\text{Vs} \end{cases} \quad (4.21)$$

It ought to be stressed that the material parameters presented here are not necessarily very close to the true values (and quite different from values found in a

standard table) for our diamond samples. To get these, more careful measurements need to be made. The purpose of extracting and presenting these parameters at all is solely to gain material to use in a model (see section 4.4.6) that makes physical sense and, at least for low particle intensities, will recreate the real detector response with some accuracy.

4.4.6 Simulation of pCVD signal

Using the equations and parameters from the previous section along with knowing the flux of secondary charged particles in time from simulations and the PS machine, one can make a discretized model of the diamond current.

Simplification of readout circuit

The maximum current that can be drawn from the power supplies is a few milliamperes which is negligible compared to the several ampere current that flows through the diamond when exposed to a high flux of ionizing particles. So on a short timescale (microseconds), the initially fully charged reservoir capacitor can be considered the only voltage source in the circuit. The $1\text{ M}\Omega$ resistor in parallel with the $50\ \Omega$ resistor (cable characteristic impedance and oscilloscope input) is replaced with a $50\ \Omega$ resistor. Another adjustment is to split up the diamond in two parallel coupled parts, one for each type of charge carrier induced current and denoting these with a specific time varying resistance. The circuit can now be replaced with the simplified one as seen in figure 4.8. A voltage loop from ground

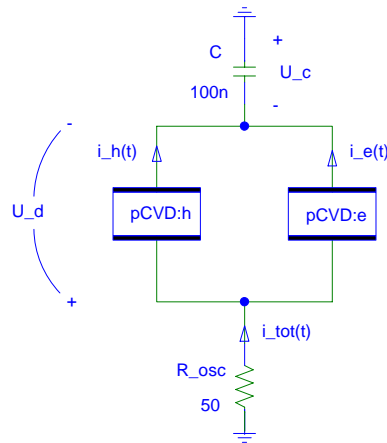


Figure 4.8. Simplified diamond detector circuit.

to ground gives:

$$U_c(t) - U_d(t) - R_{osc}i_{tot}(t) = 0 \Leftrightarrow U_d(t) = U_c(t) - R_{osc}(i_h(t) + i_e(t)) \quad (4.22)$$

Drift velocity vs. internal charge

The induced current for a group of drifting holes (n in total) in the diamond at a given moment is given by:

$$i_h(t) = nq_e \frac{\nu_h}{d} = Q_{r,h} \frac{\nu_h}{d} = \frac{Q_{r,h}}{d} \cdot \frac{\mu_h E_d}{1 + \frac{\mu_h E_d}{\nu_{h,s}}}; \quad E_d = \frac{U_d}{d}$$

$Q_{r,h}$ is the remaining hole charge inside the diamond and, unless compensated by incoming MIPs, this will decrease according to charge lifetime and when a hole reaches the cathode side. Identifying the drift velocity gives:

$$\nu_h = \frac{\mu_h U_d}{d \left(1 + \frac{\mu_h U_d}{d \nu_{h,s}}\right)} = \frac{\mu_h U_d}{d \beta_h}; \quad \beta_h = 1 + \frac{\mu_h}{d \nu_{h,s}} [U_c - R_{osc}(i_h + i_e)] \quad (4.23)$$

Further expansion:

$$\begin{aligned} \nu_h &= \frac{\mu_h}{d \beta_h} \left[U_c - \frac{R_{osc}}{d} (\nu_h Q_{r,h} + \nu_e Q_{r,e}) \right] \Leftrightarrow \\ \nu_h \frac{d \beta_h}{\mu_h} &= U_c - \frac{R_{osc}}{d} \nu_h Q_{r,h} - \frac{R_{osc}}{d} \nu_e Q_{r,e} \Leftrightarrow \\ U_c &= \nu_h \left[\frac{d \beta_h}{\mu_h} + \frac{R_{osc}}{d} Q_{r,h} \right] + \nu_e \frac{R_{osc} Q_{r,e}}{d} \end{aligned} \quad (4.24)$$

Corresponding expression for the electrons:

$$U_c = \nu_e \left[\frac{d \beta_e}{\mu_e} + \frac{R_{osc}}{d} Q_{r,e} \right] + \nu_h \frac{R_{osc} Q_{r,h}}{d} \quad (4.25)$$

$$(4.24) - (4.25) \Rightarrow \nu_h \frac{d \beta_h}{\mu_h} - \nu_e \frac{d \beta_e}{\mu_e} = 0 \Leftrightarrow \nu_e = \frac{\beta_h \mu_e}{\beta_e \mu_h} \nu_h \quad (4.26)$$

$$\begin{aligned} (4.26) \text{ in } (4.24) \Rightarrow \nu_h \left[\frac{d \beta_h}{\mu_h} + \frac{R_{osc} Q_{r,h}}{d} + \frac{\beta_h \mu_e}{\beta_e \mu_h} \cdot \frac{R_{osc} Q_{r,e}}{d} \right] &= U_c \Leftrightarrow \\ \nu_h &= \frac{U_c}{\frac{d \beta_h}{\mu_h} + \frac{R_{osc}}{d} \left(Q_{r,h} + \frac{\beta_h \mu_e}{\beta_e \mu_h} Q_{r,e} \right)} \end{aligned} \quad (4.27)$$

This gives the drift velocity for a given amount of internal charge carriers and capacitor voltage. Of course, the expression is a bit convoluted, since β_h and β_e themselves depends on ν . Interpreting β as a diamond property when calculating the current at time t , one could simply use the β -value for time $t - \Delta t$, Δt being the minimal time step, given that the changes in MIP intensity are not too dramatic

to have a fair approximation. One thing can immediately be read out of the expression. If the amount of charge in the diamond is large ($Q_r \rightarrow \infty$), the drift velocity tends to zero. This is because the maximum possible current is limited by the bias voltage (500 V) and the oscilloscope input impedance (50 Ω). The larger the number of free charge carriers, the slower they must drift not to exceed this upper current limit.

Another neglected effect here is the charge carriers screening effect on the accumulated charge on the contact surfaces. This reduces the effective internal electric field and thus yields lower drift velocities if the amount of internal charge is large enough.

Internal charge distribution

To facilitate a time discrete model, some help variables are introduced. From simulations of the number of charged secondary particles per beam proton and known proton beam bunch structure, one can calculate the frequency of incoming MIPs on the diamond surface $f_{MIP}[t_i]$ ⁵, measured in MIPs per second. This can be interpreted as a total of n bunch packets or slices, each with their individual intensity, delivered at different times. From f_{MIP} , one can define another vector, $\eta_h[k_i^h]$:

$$\eta_h[k_i^h] \equiv f_{MIP}[t_i] \Delta t \rho_{ion} q_e \quad (4.28)$$

where Δt is the length of the time step and ρ_{ion} is the number of electron hole pairs per meter created by a MIP. The independent variable is denoted k_i^h since the above definition is only an initialization value; η_h will later change with time (so it is really a square matrix, $\eta_h[k_i^h, t_j]$) and the initialization applies for $t_j = 0$. Subscript/superscript h denotes, as usual, holes as the charge carrier of interest. Similar vectors are initialized for the electrons.

Next, we introduce $\zeta[k_i^h]$ defined as the total length a given slice of charge has drifted (see figure 4.9).

The total hole charge inside the diamond at time t_j is given by adding the area of each slice (index t_j omitted):

$$Q_{r,h} = \sum_{i=k_{min}^h}^{k_{max}^h} \eta_h[k_i^h] (d - \zeta_h[k_i^h]) \quad (4.29)$$

The markers k_{min}^h and k_{max}^h indicates which charge slices has been injected into the diamond (k_{max}^h) and which has been completely extracted from it by reaching the left edge at $x = 500 \mu\text{m}$ ($k_{min}^h + 1$). Here is the reason why bothering to have different superscript (k_i^h, k_i^e) for electrons and holes: since their drift velocities are different, a group of electrons generated at the same time as their hole counterparts may still be drifting inside the diamond and induce a current after the holes have been extracted from the detector.

⁵Here, the \square denotes a vector as a function of a discrete variable - time in this case.

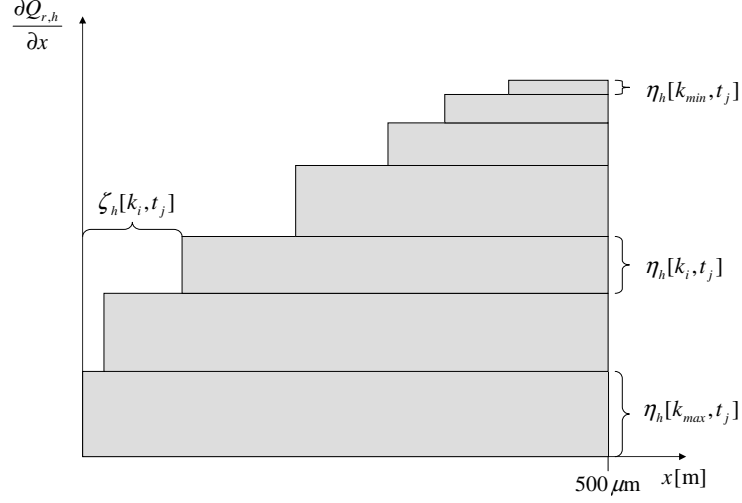


Figure 4.9. The internal charge distribution (holes) in the diamond at time $t = t_j$.

Pseudo code for current computing algorithm

Following steps are performed at each t_j :

1. “Decay” the present internal charge according to:

$$\begin{aligned} \eta_h[k_i^h, t_j] &= \eta_h[k_i^h, t_{j-1}] e^{-\frac{\Delta t}{\tau_h}} & k_i^h &\in [k_{min}^h, k_{max}^h - 1] \\ \eta_e[k_i^e, t_j] &= \eta_e[k_i^e, t_{j-1}] e^{-\frac{\Delta t}{\tau_e}} & k_i^e &\in [k_{min}^e, k_{max}^e - 1] \end{aligned} \quad (4.30)$$

2. Calculate the total internal charge.

$$\begin{aligned} Q_{r,h}[t_j] &= \sum_{k_i^h=k_{min}^h}^{k_{max}^h-1} \eta_h[k_i^h, t_j] (d - \zeta_h[k_i^h, t_j]) \\ Q_{r,e}[t_j] &= \sum_{k_i^e=k_{min}^e}^{k_{max}^e-1} \eta_e[k_i^e, t_j] (d - \zeta_e[k_i^e, t_j]) \end{aligned} \quad (4.31)$$

3. Add charge due to incoming minimum ionizing particles at time t_j

$$\begin{aligned} Q_{r,h}[t_j] &= Q_{r,h} + \eta_h[k_{max}^h, t_j] \cdot d \\ Q_{r,e}[t_j] &= Q_{r,e} + \eta_e[k_{max}^e, t_j] \cdot d \end{aligned} \quad (4.32)$$

4. Calculate $\beta_h[t_j]$ and $\beta_e[t_j]$:

$$\begin{aligned}\beta_h[t_j] &= 1 + \frac{\mu_h}{d\nu_{h,s}} (U_c[t_{j-1}] - R_{osc}(i_h[t_{j-1}] + i_e[t_{j-1}])) \\ \beta_e[t_j] &= 1 + \frac{\mu_e}{d\nu_{e,s}} (U_c[t_{j-1}] - R_{osc}(i_h[t_{j-1}] + i_e[t_{j-1}]))\end{aligned}\quad (4.33)$$

5. Calculate drift velocities at time t_j :

$$\nu_h[t_j] = \frac{U_c[t_{j-1}]}{\frac{d\beta_h[t_j]}{\mu_h} + \frac{R_{osc}}{d} \left(Q_{r,h}[t_j] + \frac{\beta_h[t_j]\mu_e}{\beta_e[t_j]\mu_h} Q_{r,e}[t_j] \right)} \quad (4.34)$$

$$\nu_e[t_j] = \frac{\beta_h[t_j]}{\beta_e[t_j]} \frac{\mu_e}{\mu_h} \nu_h[t_j] \quad (4.35)$$

6. Move each charge slice a distance forward according to their drift velocities: $l = \nu \cdot \Delta t$. If a charge slice reaches the anode/cathode side, increase k_{min} with 1.

$$\begin{aligned}\zeta_h[k_i^h, t_j] &= \zeta_h[k_i^h, t_{j-1}] + \nu_h[t_j] \cdot \Delta t; & k_i^h &\in [k_{min}^h, k_{max}^h] \\ \zeta_e[k_i^e, t_j] &= \zeta_e[k_i^e, t_{j-1}] + \nu_e[t_j] \cdot \Delta t; & k_i^e &\in [k_{min}^e, k_{max}^e]\end{aligned}\quad (4.36)$$

7. Update the current flowing through the diamond

$$\begin{aligned}i_h[t_j] &= Q_{r,h}[t_j] \frac{\nu_h[t_j]}{d} \\ i_e[t_j] &= Q_{r,e}[t_j] \frac{\nu_e[t_j]}{d}\end{aligned}\quad (4.37)$$

8. Reduce the voltage over the capacitor

$$\begin{aligned}C \cdot \frac{\Delta U_c}{\Delta t} = i &\Leftrightarrow \Delta U_c = (i_h + i_e) \frac{\Delta t}{C} \Rightarrow \\ U_c[t_j] &= U_c[t_{j-1}] - (i_h[t_j] + i_e[t_j]) \frac{\Delta t}{C}\end{aligned}\quad (4.38)$$

9. Increase k_{max}^h and k_{min}^e with 1 to add more e-h pairs in the next iteration.

Simulation results for different parameters

At an early stage, the major concern is at which levels one can expect that the diamonds start to show saturation effects; that is, the rate of created electron-hole pairs is higher than what the bias voltage can manage to drain. When this happens, the linearity between the integrated charge and the number of incoming MIPs breaks down. As the extracted diamond parameters are a bit uncertain, the lifetime can be set to higher than assumed while calculating the diamond current for a given number of MIPs arriving during 50 ns. Should the current approach the maximum (10 A) one should be aware that a detector subjected to such a flux will not behave linearly.

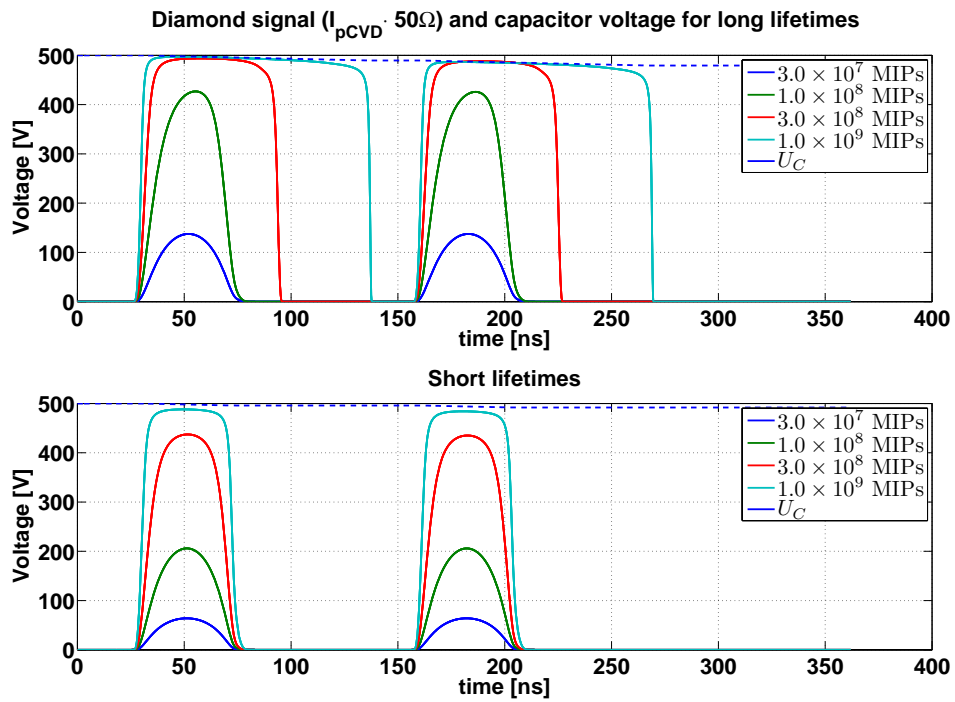


Figure 4.10. Simulation of diamond signal (current over a $50\ \Omega$ resistor) for different charge carrier lifetimes. The voltage drop is calculated for 10^9 MIPs. Upper: $\tau_h = 20$ ns, $\tau_e = 60$ ns. Lower: $\tau_h = 0.9$ ns, $\tau_e = 2.7$ ns.

Figure 4.10 shows the simulated current for different charge carrier lifetimes and number of MIPs. The time distribution of MIPs is assumed to be proportional to a roughly Gaussian bunch spill with 50 ns width. The lower graph is calculated using the lifetimes extracted in this chapter, while the upper is calculated using - for polycrystalline diamond - unrealistically long lifetimes⁶. For the long lifetimes, we see that for a large number of MIPs, the amount of generated charge is too high for the read out circuit to effectively drain the diamond of free charge carriers and the internal charge increases as long as MIPs are traversing the diamond. As the flow of MIPs ceases, there is still a lot of charge inside the diamond that continues to generate a current, long after the last ionizing particle has created any electron hole pairs. The short-lifetime-case shows significantly narrower signals since the internal charge in this case quickly gets trapped (“decays”) as soon as there is no more ionizing radiation. For low fluxes of MIPs, the long lifetimes gives voltage peaks about double that of the short lifetimes.

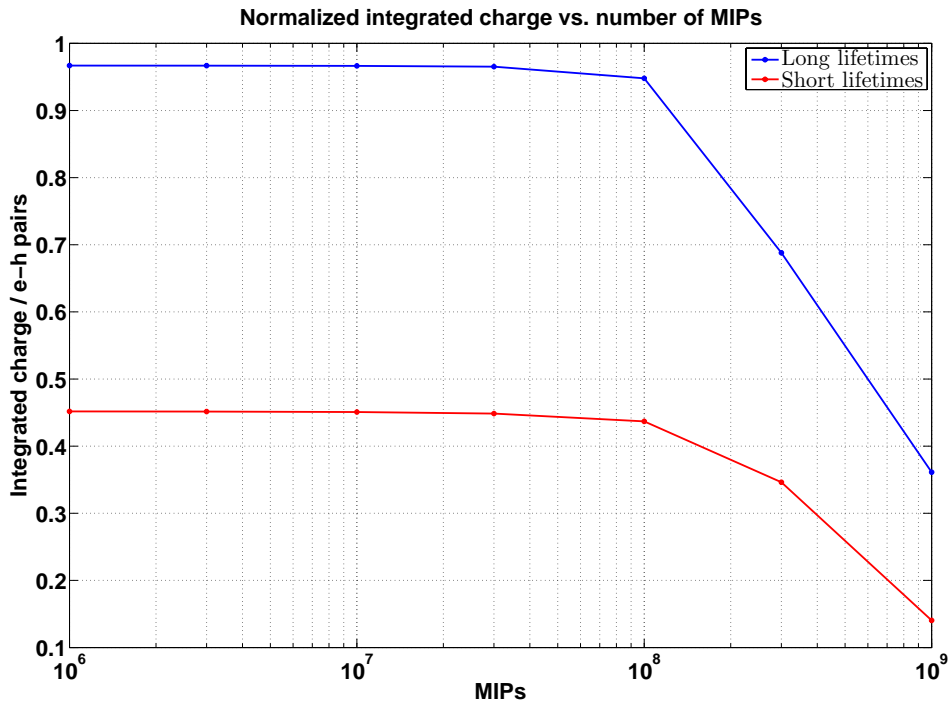


Figure 4.11. Integrated charge (elementary charges) divided by number of created electron-hole pairs.

By plotting the integrated charge versus generated number of e-h pairs (see figure 4.11), one can see up to which levels a diamond behaves linearly. For an infinite lifetime, the normalized integrated charge should be identical to 1, meaning no charge loss during extraction. This is almost the case for the long lifetime up

⁶They are closer to what could be expected of a single crystalline diamond (sCVD).

to 10^8 MIPs. Regardless of the lifetimes, both parameter configurations behave linearly up to about 10^8 MIPs.

Chapter 5

Performance test of detectors

5.1 pCVD in high intensity proton beam

The diamonds have previously been shown to withstand high intensities of charged particles while giving a reliable output[8]. Shown in figure 5.1 is the response of one detector subjected to eight bunches of 10^8 protons/cm². Each bunch lasts for 40 ns and the detector is biased at 1 V/ μ m, so the conditions are very much like those expected in MERIT. The variation in peak amplitude follows well the variation in bunch intensity.

5.2 ACEM in dipole magnet

5.2.1 Setup

To verify that the shielding (6 cylindrical layers of 1 mm μ -metal plus a 10 mm thick iron cylinder) around the tube is enough for the detector to still function in the vicinity of the MERIT solenoid, the whole detector was placed inside a dipole magnet in the North Area along an extraction line from the SPS accelerator. Right on top of the detector is a β -source (⁹⁰Sr). Since the energy of the emitted electrons is quite low, the innermost layer of the μ -metal had to be replaced with a paper tube covered with thin, black tape. By varying the current of the magnet and doing double measurements for the radioactive source open and closed, one can directly see how the B-field affects the photomultiplier. One effect that has been neglected here is that the magnetic field also affects the emitted electrons by Lorentz force. This is partly compensated by simply sliding the outermost layer of μ -metal over the Sr-sample.

To keep the detector from being hurled away due to the strong magnetic field it has been tightly secured under a steel frame (when B-field is perpendicular to detector axis) or hold in position by lead bricks (when B-field is parallel to detector

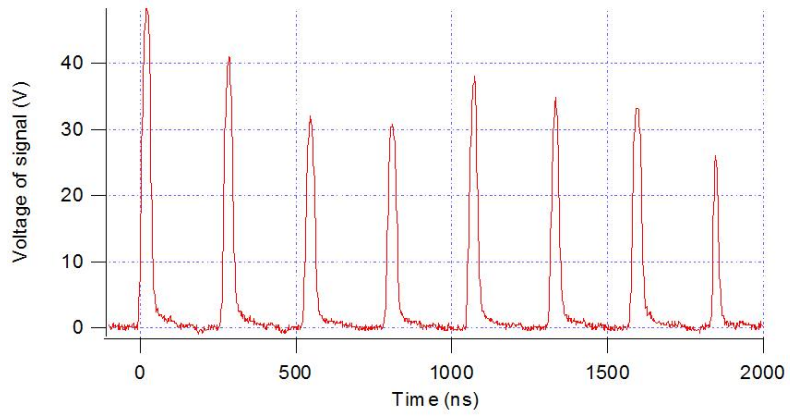


Figure 5.1. Multi-bunch response from a diamond detector at high intensity.

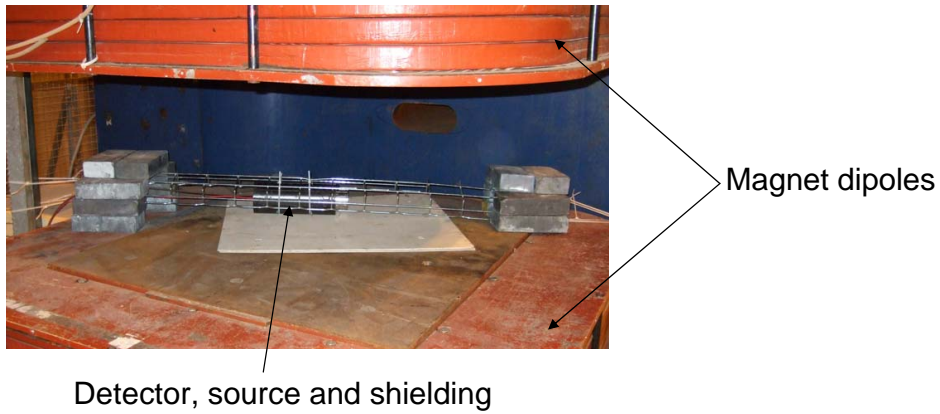


Figure 5.2. One of the ACEM detectors inside a dipole magnet, aligned perpendicular to the magnetic field.

axis). The detector was biased at 1100 V and the output signal connected to a discriminator set to trigger at 60 mV, which is sufficiently high to block triggers due to noise from the electronics. Any cosmic background radiation is still easily picked up by the ACEM and gives about half as many triggers as the source.

During two minutes, the number of triggered events was counted at different magnetic field strengths. Initially, the current was increased until no triggers were registered and then lowered to zero again. The magnetic field for the dipole used is given by:

$$B = kI; \quad k = 6.61 \text{ G/A} \quad (5.1)$$

5.2.2 Results

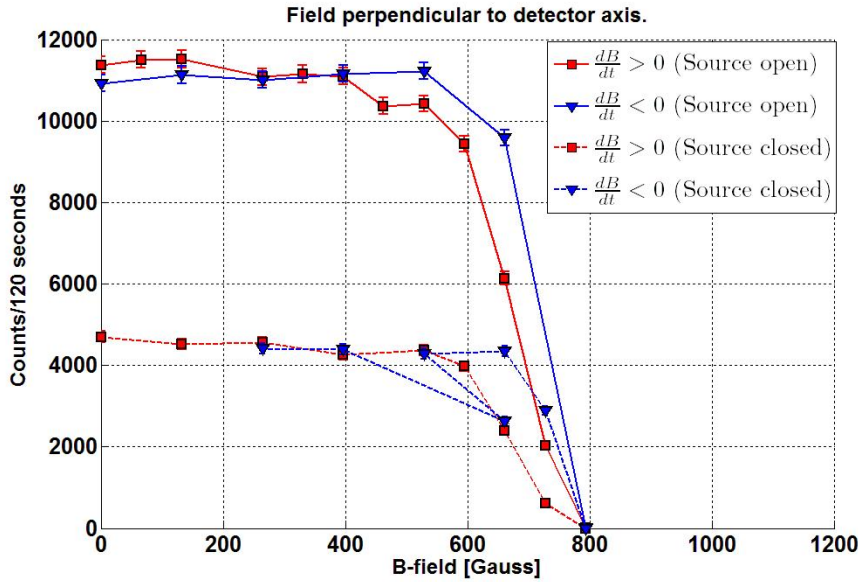


Figure 5.3. Number of counts per 2 minutes vs magnetic field strength. Magnetic field is perpendicular to detector axis. $\frac{dB}{dt} > 0$ indicates an increase of the magnetic field with respect to the previous measurement. $\frac{dB}{dt} < 0$ indicates a decrease (except for one point at 650 G).

It is clear that the ACEM detector is practically unaffected by the magnetic field up to 500 Gauss when the magnetic field axis is perpendicular to the detector. This corresponds to a distance of less than three meters behind or in front of the solenoid.

The case when the magnetic field is aligned with the detector is fundamentally different and there is an almost linear decrease of the discriminator trigger frequency. Not surprisingly, the shielding is quite ineffective in absorbing magnetic field lines oriented along the detector axis. Luckily, most of the ACEM detectors will not be oriented like this. The one closest to the solenoid will be looking in

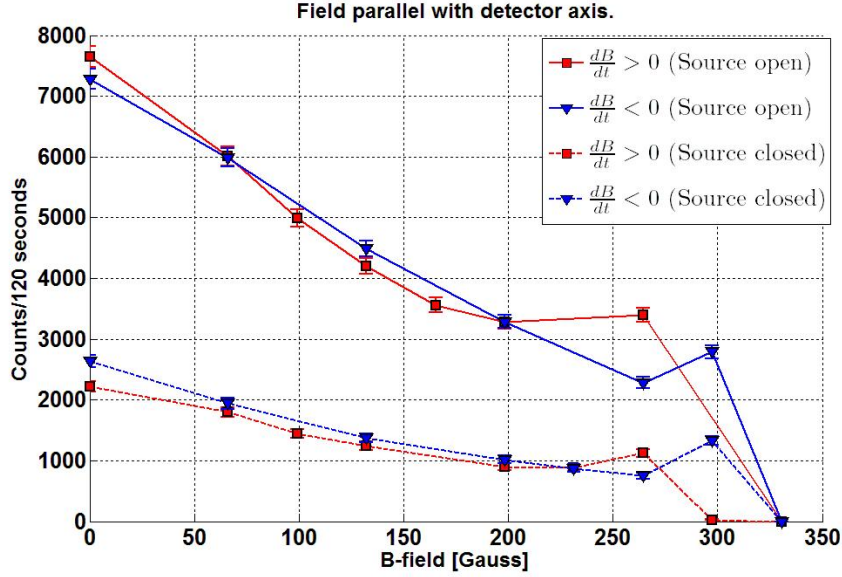


Figure 5.4. Number of counts per 2 minutes vs magnetic field strength. Magnetic field parallel to detector axis.

to the solenoid at a 90 degree angle and thus having the field completely perpendicular to the shielding. One should have in mind though, that the source itself in this testing is only shielded with 1 mm μ -metal which reduces the number of electrons reaching the ACEM cathode, and that the PM-tube lacks the top layer of protective μ -metal.

One curiosity is the little “hump” that is visible at the high field end for the parallel case. This might be explained by the electrons at this level being subjected to just enough Lorentz forces to complete a large enough fraction of a revolution that they manage to reach the following dynode. A very rough calculation where we approximate the distance d between two dynodes to 1 cm and assume the voltage V to be evenly distributed over the ten dynodes gives the time to go from one dynodes to the next to:

$$t = \frac{d}{v} = \frac{d}{\sqrt{\frac{2E_k}{m_e}}} = \frac{d}{\sqrt{\frac{2q_e(V/9)}{m_e}}} = 1.5 \text{ ns} \quad (5.2)$$

The cyclotron frequency for the electrons in a magnetic field B of 300 G is given by:

$$\omega_c = B \frac{q_e}{m_e} = 5.3 \cdot 10^9 \text{ rad/s} \quad (5.3)$$

As the product $\omega_c t = 7.8 \text{ rad} \approx 1.2 \text{ revolutions}$ is fairly close to one complete revolution this hypothesis is not unreasonable if the shielding efficiency is poor with the detector parallel to the field.

The number of counts are plotted with a 95 percent confidence interval (Gaussian distribution) so the big differences at some data field between the increasing and decreasing current curves can not be dismissed as statistical fluctuation of the source activity. In general, the decreasing field-curves have a higher trigger rate at magnetic fields close to where the detector stops functioning. This observation is not understood, although it looks like it takes longer for the magnet to adapt to the new current level than is indicated at the operator interface.

Chapter 6

Experimental setup

This chapter presents a brief overview of the peripheral equipment and software employed to serve the particle detectors during operation. The underlying philosophy has been to make as much of the equipment as possible remotely controllable since the MERIT control room is located about 1 km from the experimental area in the TT2 tunnel. Furthermore, the access to TT2 is limited since this is a protected radiation zone, meaning that the PS can not operate as long as there are people working inside the zone. This makes a remotely controlled system not only convenient, but important if one would need to change any settings on the fly.

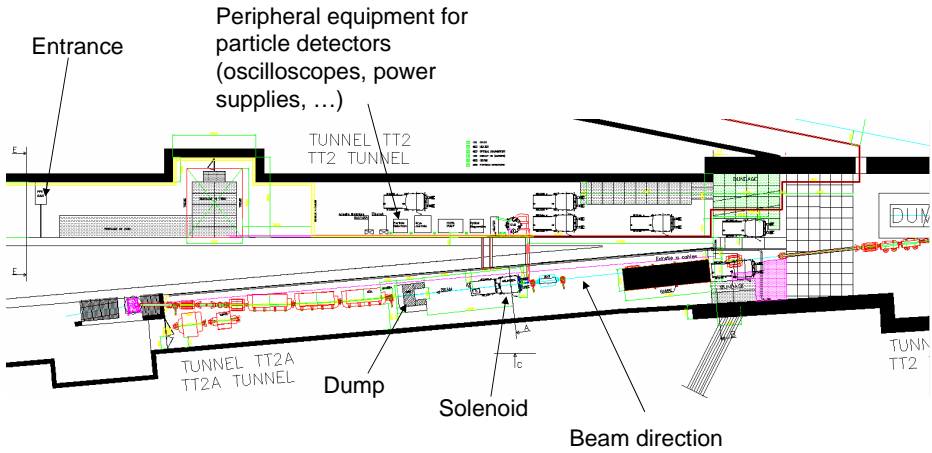


Figure 6.1. Layout of the MERIT site in the TT2 tunnel

6.1 Specifications

6.1.1 Oscilloscopes

	Tektronix 744A	LeCroy WavePro 7100
Input channels	4	4
Max sample rate	500 MS/s ¹ using 4 channels	2.5 GS/s using 4 channels
Number of divisions	10 (8 visible on display)	8
Input impedance	50 Ω /1 M Ω	50 Ω /1 M Ω
Max volt/division	1.0 V at 50 Ω	1.0 V at 50 Ω
Min volt/division	1.0 mV	2.0 mV
Resolution	8 bits	8 bits
Memory	50 kpts/ch at single acquisition	1 Mpts/ch at single acquisition
	5 kpts/ch at segmented acquisition	0.5 Mpts/ch at segmented acquisition
Bandwidth (-3 dB)	500 MHz	1 GHz
Remote control	GPIB ²	Ethernet

Table 6.1. Oscilloscope performance

Requirements for the oscilloscopes:

Sampling speed The signals from the detectors are expected to last at least as long as the proton bunches, i.e. 50 ns. To capture a good representation of these signals a minimum of 15 samples are desired, setting a lower limit for the sampling rate to 300 MS/s. But obviously, the more, the better - as long as the oscilloscope analog bandwidth³ can match the sampling speed.

Segmented acquisition As mentioned, the time between the pump bunch and probe bunch can be in the order of milliseconds. If one were to let the oscilloscopes record the entire signal from first to last micro bunch, a vast amount of memory would be required given the high sampling speed. A better way is to split up the oscilloscope memory in two segments and store a few microseconds (10 μ s in our case) of interesting signal at each pulse arrival and set the oscilloscope on hold in between. This is not a too complicated feature, but not all oscilloscopes possess it. On the considered oscilloscopes that do, this requires one extra external trigger pulse for each segment.

Remotely controllable Any reasonably modern oscilloscopes supports remote controlling. For our purposes, this is necessary to make data analysis of the acquired signals on a computer, but also to be able to change settings on the oscilloscopes without interrupting the PS beam by entering TT2 area. The Tektronix uses a GPIB protocol, requiring a direct cable from the oscilloscope

¹Megasamples per second

²General Purpose Interface Bus

³Related to the input amplifiers, among other things.

to a computer while the LeCroy is equipped with an Ethernet connection, which makes the communication speed significantly faster than with the Tektronix.

6.1.2 Pulse generator - HP81110A

To generate the double trigger pulse when the pump-probe time is long, a pulse generator has been positioned between the main trigger (which triggers the pulse generator), directly linked to the PS, and the oscilloscopes (being triggered by the signal from the pulse generator). If the pump-probe time is short enough for the rendered signal to be captured in a single interval, the pulse generator is simply set to single pulse-mode and generates an oscilloscope trigger signal when triggered by the PS signal. Should the pump-probe time be longer than some tens of microseconds⁴, the pulse generator is set to deliver two trigger pulses whose time separation matches that of the two proton pulses. Like the Tektronix oscilloscope, this is remotely controlled by GPIB with the two devices linked in a daisy chain and connected to the control PC by a GPIB-to-USB interface.

6.1.3 Power supplies - CAEN N470

Output channels	4
Number of devices	5
Output voltage	0 to ± 3 kV
Max current	3 mA

The CAENs supply the detectors with a suitable voltage (-500 Volts for the diamonds). In total there are 20 available output channels in case some should break down for one reason or the other⁵. The power supplies are provided with a High Speed CAENET interface which uses a simple 50 Ω LEMO cable as transmitter/receiver to a H.S. CAENET PC Controller module card in the control PC. This enables a fairly fast communication in programming the power supplies and reading their status during operation.

6.1.4 Attenuators

Due to the expected high current from the diamond detectors at nominal working voltage, attenuation of up to 40 dB is necessary to protect the oscilloscope inputs. The attenuators are located in the same position as the rest of the peripheral equipment and are the only devices that are not remotely controllable⁶. The implication of this is that the first runs in the experiment might be dedicated

⁴The Tektronix can sample up to 100 μ s at 500 MS/s, setting the threshold for single/segmented acquisition to slightly shorter than this time.

⁵This did happen during a hipot test of the solenoid coils.

⁶Efforts were made to find remotely controllable attenuators, but were either too expensive, had too low bandwidth or were not specified to withstand a very short high power pulse.

to find a suitable attenuation factor of each individual detector signal should the simulations and expected detector response be off by an order of magnitude.

6.1.5 Cables

As the distance from the detectors inside the experiment hall to the position of the acquisition equipment is quite long - 50 meters - the cables' damping effect on high frequencies should not be immediately dismissed. Following [9], the cable can be considered a general 2-port, which in matrix notation gives, for the voltage and current:

$$\begin{pmatrix} V_1 \\ I_1 \end{pmatrix} = \begin{pmatrix} A & B \\ C & D \end{pmatrix} \begin{pmatrix} V_2 \\ I_2 \end{pmatrix} = \begin{pmatrix} \cosh(\gamma l) & Z_0 \sinh(\gamma l) \\ \frac{1}{Z_0} \sinh(\gamma l) & \cosh(\gamma l) \end{pmatrix} \begin{pmatrix} V_2 \\ I_2 \end{pmatrix} \quad (6.1)$$

$$\gamma = \sqrt{(R + j\omega L)(G + j\omega C)} \quad (6.2)$$

R , C , G , L are cable characteristics per unit meter (e.g. $C = 84$ pF/m for the diamond detector cable⁷) and Z_0 the characteristic impedance. Next, we use the simple cable attenuation-measurement setup (see figure 6.2) for interpretation of the available attenuation numbers at different frequencies available:

Frequency [MHz]	Attenuation [dB]
1	0.5
10	1.6
100	5.1
200	7.2
800	15
1000	16.8
1600	21.7
2000	24.3
3000	30.2

Table 6.2. Cable attenuation for different frequencies.

The transfer function from the generator to the load impedance can be expressed as:

$$H(\omega) = \frac{U_L}{U_G} = \frac{Z_L}{B + AZ_L + DZ_S + CZ_L Z_S} \quad (6.3)$$

Rather than looking at this expression, which is simply equal to $1/2$ for a perfect cable if $Z_G = Z_L$, we look at $2 \cdot H(\omega)$ for $Z_G = Z_L = Z_0 = 50\Omega \equiv R$ as this expression should be close to unity for low frequencies and gives the attenuation at higher frequencies:

$$\begin{aligned} 2 \cdot H(\omega) &= \frac{2 \cdot R}{B + R(A + D) + R^2 C} = \frac{1}{\sinh(\gamma l) + \cosh(\gamma l)} = \\ &= e^{-\gamma l} = e^{-l\sqrt{(R+j\omega L)(G+j\omega C)}} \end{aligned} \quad (6.4)$$

⁷Coaxial cable, type C-50-6-1.

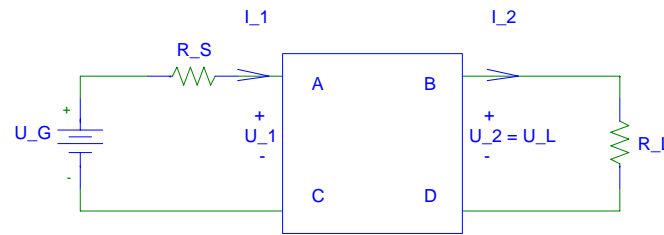


Figure 6.2. 2-port model of cable in attenuation-measurement setup

Fitting equation 6.4 to the data points yields: $R = 1.43 \text{ m}\Omega/\text{meter}$ and $G = L \approx 0$.

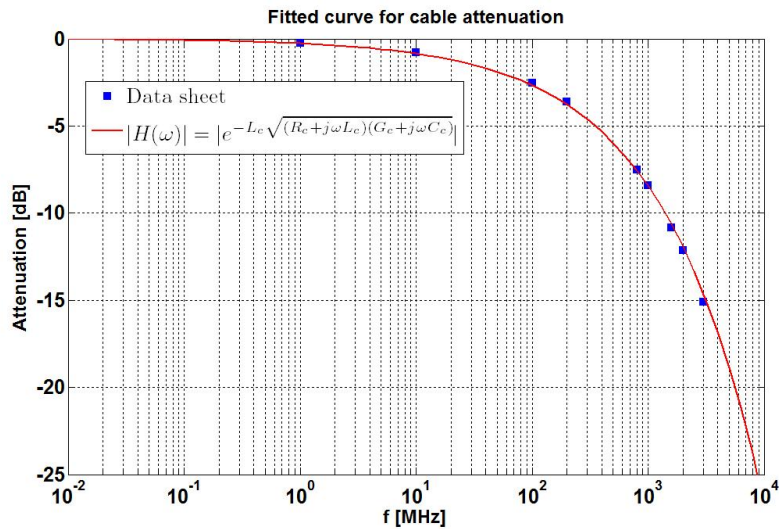


Figure 6.3. Attenuation curve fitted to data sheet for diamond detector cables.

6.2 Equipment interface

6.2.1 Instrument communication

The particle detector system is geographically divided into three parts (see fig 6.4). Inside the experimental area are all the detectors, connected by cabling to the equipment in the access tunnel: oscilloscopes, power supplies and pulse generator - all connected to and controlled by PC2. This computer can be controlled by the user from any other location with an Internet connection.

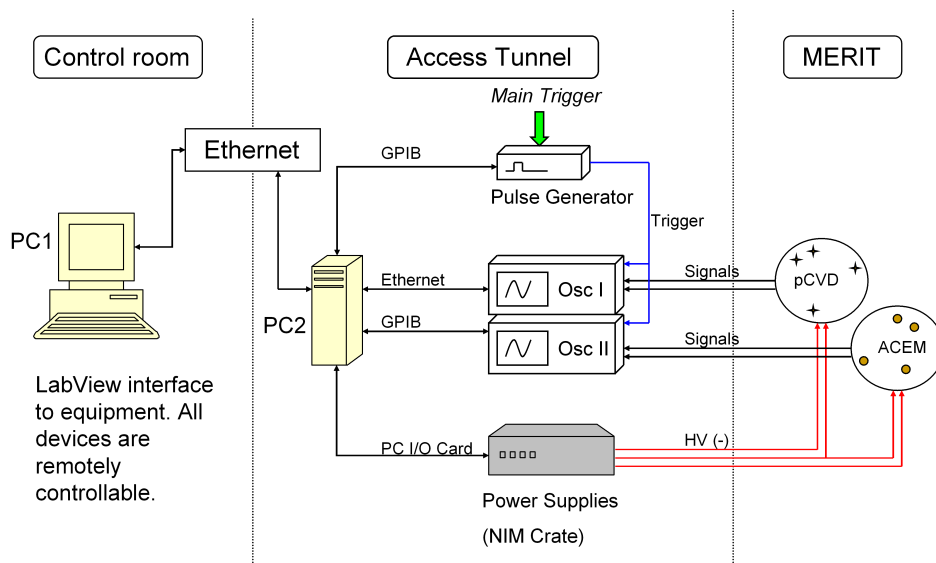


Figure 6.4. Schematics of equipment communication.

6.2.2 LabView interface

To easily control all the equipment it is necessary to create one single interface that simultaneously can handle all the different kinds of protocols and means of communication and in real time apply the desired settings or display status to quickly detect potential malfunctioning of a device. LabView is a suitable choice of software to do this as it provides many instrument drivers to common remotely controlled devices on the market.

The design philosophy in making this interface has been to implement only the functions necessary for a user to satisfactorily operate the particle detection system from any PC within the CERN network, this PC by a remote desktop control accessing the computer placed in the TT2 tunnel equipped with the necessary hardware to read and write to the peripheral equipment (see figure 6.4). Each detector is assigned an oscilloscope input and a power supply output. Below follows a short description of the implemented features.

1. Oscilloscopes

- **Range:** The maximum peak-to-peak range of the attenuated signal.
- **Offset:** How much voltage to add to the signal before it is acquired. As e.g. the diamond signals are purely negative, it allows for a better oscilloscope resolution to have the signal centered around a zero offset level.
- **Delay:** The time to wait between trigger signal from the pulse generator to start of acquisition. Should the PS trigger arrive long before (or

shortly after) the beam-mercury interaction, this can be compensated for by adjusting the internal oscilloscope delay in order not to miss any part of the detector signal.

2. Power supplies

- Voltage: The bias voltage for each individual detector. The present difference between desired and actual voltage is presented and continuously updated.
- Max current: Protective upper limit for the maximum current that can be drawn from the power supplies. In case of an unexpected short circuit somewhere between the power supply and the detector, this prevents further damages. As with the voltage, a current monitor informs the user of the present current going through the detector.
- Status fields: Several indicators presenting the status of each power supply in general (High Voltage enabled, “Kill flags”, Alarm) and output channel specific information (On/off, high current, over/under voltage, polarity, ramping up/down etc.)

3. Pulse generator

- Trigger source: External (from PS) or manual (for debugging or fault identification)
- Single/double pulse threshold: The maximum pump-probe time for the oscilloscopes to operate in single trigger mode. Should the pump-probe time be longer than this, the pulse generator delivers double triggers to the oscilloscopes who are then set to segmented acquisition mode.

4. Signal display. After a trigger, the TT2 computer loads the signals from the oscilloscopes and stores them on the hard drive whereupon the responses from each activated detector are displayed on the screen. Based on this, the user can quickly decide whether anything has to be adjusted, such as increasing the voltage to one of the ACEM detectors if its signal is weaker than anticipated.

5. Other parameters like detector attenuation or PS harmonic are strictly speaking not necessary for the data capture to work, but the user is still encouraged to type these in as they are important for the future analysis of the data.



Figure 6.5. Snapshot of the LabView interface to the particle detectors

Chapter 7

FLUKA simulations

The simulations discussed in section 3.2 are made using MARS¹. The accuracy of these kinds of simulations is typically about 30%, therefore it would be wise to cross check the results with an equivalent simulation scenario using a different software. For this purpose, I have used a CERN developed MonteCarlo simulation package called FLUKA[5][6]. The program operates by injecting the desired type of beam, or primary particles, (protons in our case) particle by particle into an environment. By using a random number generator and a statistical library, with particle properties and cross sections for different interactions, each particle will “randomize” it’s way through the geometry, yielding secondary particles and deposit energy. When this is done for a large number of primary particles, the statistical outcome of the simulation will reminiscent the reality.

The object of these simulation is mainly to confirm the previous results but also to simulate other scenarios, such as what happens to the angular distribution of the secondary flux if the proton beam is slightly deviated from the center of the mercury target.

7.1 Geometrical model

In order to do any simulations at all, one must obviously model the geometry. Included should be all objects that are subject to high instantaneous radiation doses from a Hg/proton interaction. The following objects have been included in this model:

- Mercury target
- Secondary mercury container
 - Including titanium beam windows upstream and downstream of the interaction point
- Snout

¹See <http://www-ap.fnal.gov/MARS/>

- Solenoid
- Beam dump
 - Consisting of iron and concrete blocks
- Primary mercury container
- Tunnel walls, floor and ceiling

The user routines for geometry modeling in FLUKA are a trifle primitive, but sufficient. All objects are built up by boolean operations² on simple building blocks: parallelepipeds, cylinders, spheres, cylinders, cones or wedges etc. forming regions. Once the geometry is completed one assigns a material to each region (e.g. mercury or vacuum). Surrounding the entire geometry is a region called “Blackhole”, annihilating all entering particles to avoid particle tracking too far away from the positions of interest.

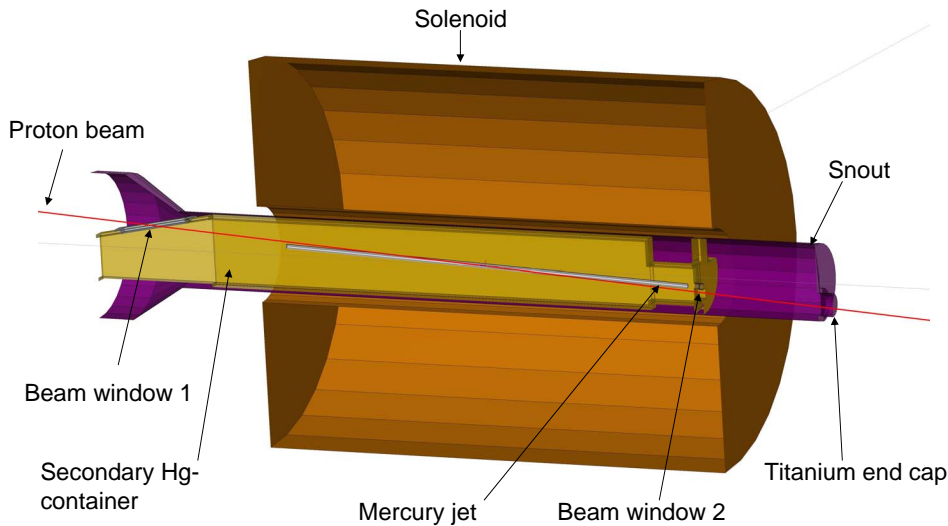


Figure 7.1. Cross section of solenoid. Beam trajectory along red line, from right to left.

7.2 Simulation objectives

The main objective of the simulations is to confirm the ones previously made with a different program. This includes simulation of different kinds of charged particles (MIPs) incident on a detector. Other parameters of interest is the asymmetry in particle production due to a possible misalignment of the beam, or the target. Should the beam be slightly off center relative the mercury jet, the secondary particles produced can be biased in either direction, causing an amplitude difference between the signals in two otherwise symmetrically placed detectors.

²Unions, subtractions or intersections

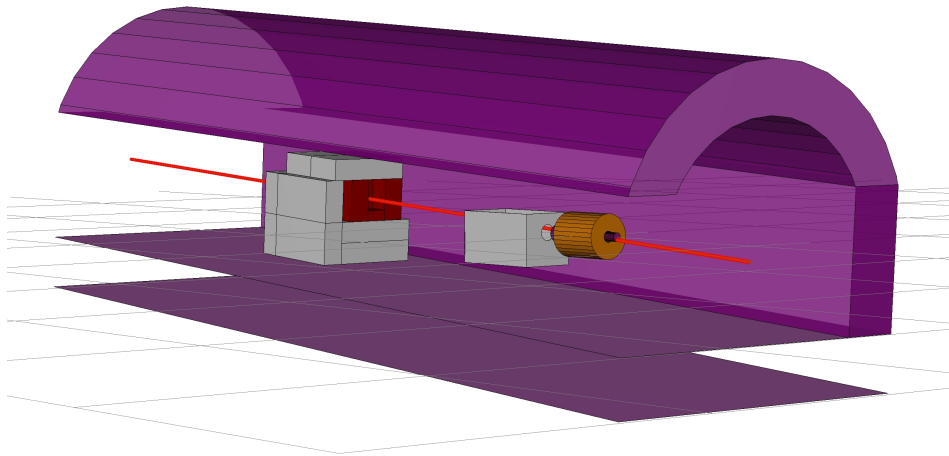


Figure 7.2. Model of the MERIT tunnel and relevant inventory.

7.3 Results

7.3.1 Flux of charged particles, MARS and FLUKA

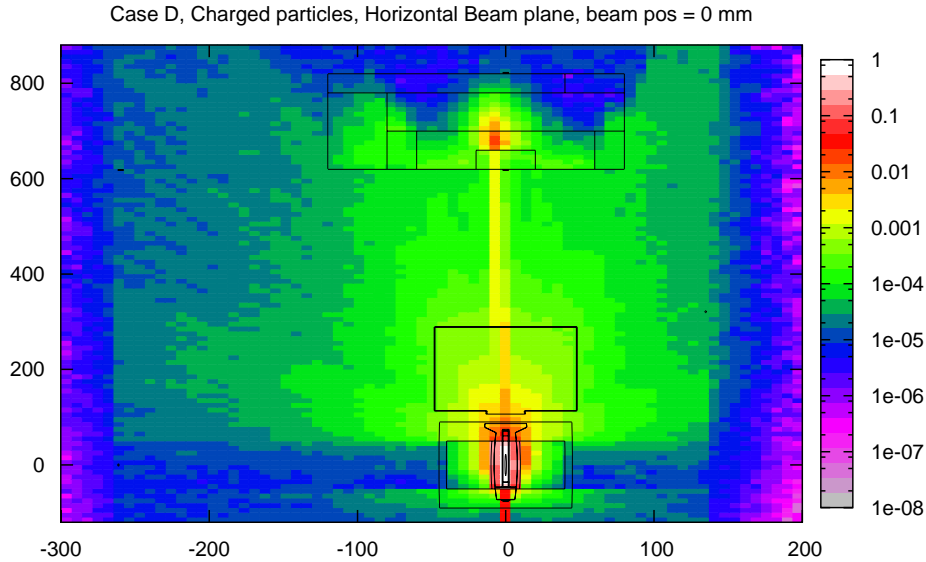


Figure 7.3. Flux of charged particles (per cm^2) in the horizontal beam plane. Mercury target is in, magnetic field 15 Tesla and the beam is centered on the jet.

To verify that the two simulation methods are in agreement, we look at the flux of charged particles at a few different geometrical points corresponding to detector positions (see figure 4.1) as these numbers are very important when estimating the total signal from the diamond detectors. As seen in table 7.1, the results are in very good agreement.

Detector position	FLUKA	MARS
Left 20°	$1.5 \cdot 10^{-5}$	$1.5 \cdot 10^{-5}$
Left 7.5°	$5.8 \cdot 10^{-5}$	$5.4 \cdot 10^{-5}$
Right 7.5°	$6.2 \cdot 10^{-5}$	$5.7 \cdot 10^{-5}$
Right 20°	$4.3 \cdot 10^{-5}$	$4.8 \cdot 10^{-5}$

Table 7.1. Comparison; FLUKA and MARS fluxes [MIPs/ cm^2 /proton] in a 24 GeV/c simulation.

7.3.2 Proton beam bending

As the proton beam enters the magnet, it will experience a small magnetic “kick” due to the tilting angle of the solenoid. In reality, there will be stray fields from

the solenoid extending several meters, but as a proper model of these is far from trivial, the magnetic field in the FLUKA simulations has been defined to be solely inside the solenoid and completely homogeneous directed along the solenoid axis in the beam direction. To visualize the bending effect on the proton beam, a fine-meshed binning has been applied inside the solenoid to log the proton flux at 15 T. The mercury jet target has been replaced with vacuum in this simulation to get a clearer view of the beam trajectory and the number of primaries are low as we are not interested in any particle production statistics. As predicted with

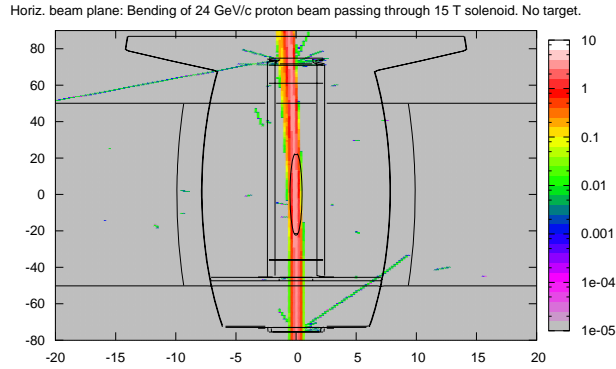


Figure 7.4. Magnetic bending of a 24 GeV/c proton beam in 15 Tesla.

the “right-hand-rule” for the Lorentz-force, the proton beam deviates to the left when entering the solenoid. The angle is not very big (the magnetic kick is about $15 \cdot \sin(0.022) \cdot 1.00$ Tm, where 0.022 is the angle between beam and solenoid axis), but could bias a the flux of secondaries in the left direction. The effect is also seen in figure 7.3, where the remnant beam is not centered on the beam dump.

7.3.3 Asymmetry

When running the experiment, there is no precise way of telling exactly where on the mercury jet the beam hits. Apart from relying on a careful placement of the mercury jet system, it would be good to know what the flux of secondary particle would look like if the beam and jet are slightly displaced. If the beam is off by a few millimeters to the right or left of target center, this could be manifested as an asymmetry in particle flux for, say, the two detectors placed on the dump. A scan of the beam from -5 to +5 millimeters from target center has been simulated to see if the impact on the detectors is big enough to reliably tell that, in the real experiment, the beam should be moved more to the right or left. For each beam position, the relative asymmetry (here defined as the difference in MIP flux, charged particles per centimetre squared, between left and right, divided by total MIP flux on the two detectors). From figure 7.5 we conclude that plus or minus two millimeters should not matter that much in terms of total particle yield. On the other hand, there is a clear trend showing that as the beam is displaced to the

left, the detector on the left side of the dump receives more secondaries and vice versa. As for the magnitude of this asymmetry, the statistics is not good enough to give a “smooth” curve - or even error bars confined on the plus or minus side - but based on the figure one would expect about 10% more signal for the right (left) detector if the beam is displaced by some 2 millimeters to the right (left).

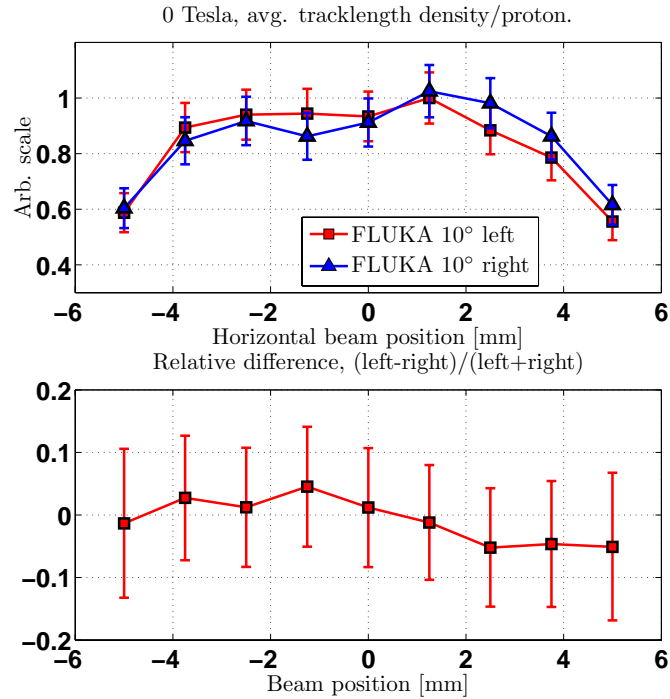


Figure 7.5. Relative flux on the two diamonds on dump front and asymmetry at 0 Tesla.

Now, if we turn the magnetic field on (15 Tesla) and do the same plot (figure 7.6) we see some interesting differences. First, the symmetry around the beam centered position is broken and secondly, the left detector receives slightly more than the right one for almost all beam position. Both effects can be understood by looking at figure 7.4. It seems plausible that a beam tending to the left would cause more secondaries to do the same. Also, the slight curvature of the beam trajectory inside the solenoid will have a greater impact on the particle production if the beam is shifted to the left than the right (when shifted to the right, the production rate is somewhat compensated by the beam turning into the target at a later time). Unfortunately, the magnet will also have an unfocusing effect of the secondaries. Particles with different momentum will change their direction differently and the large fluctuations of the asymmetry seen in the figure are not useful in making any positive statements.

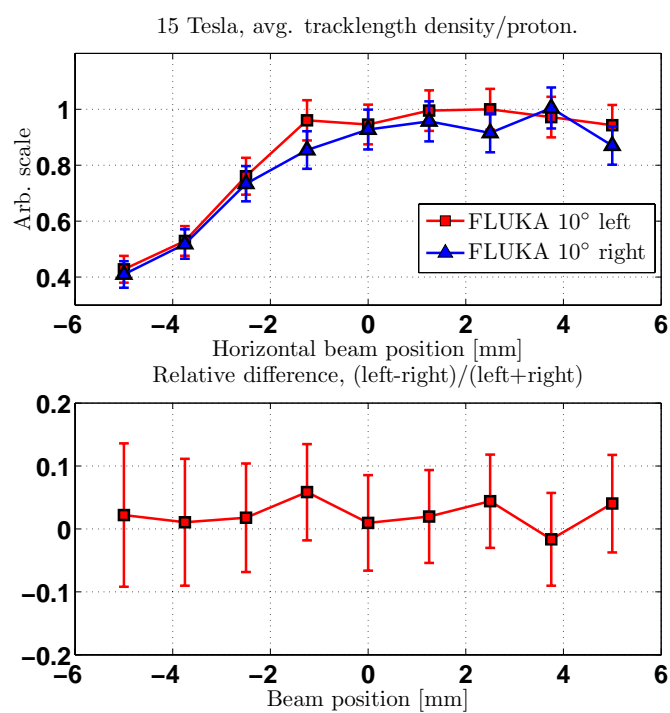


Figure 7.6. Relative flux on the two diamonds on dump front and asymmetry at 15 Tesla.

Chapter 8

Results and observations from the MERIT run

8.1 Experimental run

The MERIT run took place during October 23 to November 11 and was executed by two groups; one on the Swiss CERN site where the solenoid, cryogenics and optical diagnostics were monitored, the other in the CERN Control Center on the French site, operating and surveilling the particle detectors, PS beam and extraction line with current transformer and beam windows to MERIT. The highest achieved proton intensity was 30 TP at Harmonic 16 with a momentum of 24 GeV/c, setting a new record in PS beam energy.

At most, there were eight detectors active simultaneously (limited by the number of available digitizing channels). Of the three types available the diamonds were by far the most reliable: several ACEMs were possibly suffering from saturation and showed very long remnant tails, although the bunch structure were more or less clear. The PIN-diode responses did not hold a good enough quality to deserve any input channels. One of the diamond detectors, initially at 90 degrees, was moved to the snout for beam guiding purposes. This position is directly in the beam line, upstream of the target and the particle flux is several orders of magnitude higher than at the other detector positions. As predicted by the diamond simulations, the detector showed clear saturation behavior - the signal rising to almost the bias voltage and with a HWFM much longer than for the other diamonds. For multi-bunch extractions, there was also a clear discharge of the reservoir capacitor, resulting in successively lower peaks. A full analysis and understanding of the diamond response at these intensities is beyond the scope of this thesis.

8.2 Data analysis

As mentioned, the key parameter to extract from the detector signals is the integrated bunch responses, ideally being proportional to the amount of yielded secondary particles for each bunch. Due to possible detector saturation and limited charge lifetime, this proportionality may not hold for high intensities, worsening with an increasing number of MIPs interacting with the detector. As LabView is not very feasible to make more complex analysis of data, it is only used to do simple on-the-fly analysis directly after each beam extraction, such as integrated signal per bunch and peak voltage. More rigorous treatment of the data is made with Matlab.

8.2.1 Linear offset

The detector signals in stand-by mode may drift a little up or down as the 50 m long cables pick up electrical noise. This could obscure the integration of the bunches, so any initial signal offset from the zero-level is removed by subtracting the average of the first microsecond from the entire signal.

8.2.2 Bunch integration

As the bunch-to-bunch time is known from the PS, the only unknown parameter is where the first integration limit should be placed. The rest are added according to known inter-bunch spacing and pump-probe time. Due to different cable length, minor differences in response time between different detector types and different behavior of the PS accelerator for different beam configurations, this is not the same for every detector in a run or for individual detectors between runs. In order to find the integration limits, a reference signal, $U_{ref}(t)$, is constructed, having the same time profile as an ideal proton beam with the known time between each micro-bunch. Using this, one then tries to find the maximum point for:

$$\min_{t_0} \int U_{ref}(t - t_0) \cdot U_{sign}(t) dt \Rightarrow \frac{\partial}{\partial t_0} \int U_{ref}(t - t_0) \cdot U_{sign}(t) dt = 0 \quad (8.1)$$

Or, in other words, trying to find the optimal time shift t_0 that maximizes the integrated area. In principle, this should correspond to a time shift that makes the reference function overlap the signal. Once the integration intervals are chosen, the next problem is to take care of possible signal tails, spilling over from one bunch response into the next when having more than one micro bunch in the beam extraction. This can be done by looking at the detector responses for several single-bunch runs and make an approximative fit of how many percent of the complete signal is to be found in the integration intervals following the main one¹. Having these coefficient one can simply make an inverse calculation to estimate the detector response for each micro bunch that needs to be correlated to the actual

¹As the diamond detectors have a fall time of a few nanoseconds, this is not expected to be more than a few percent - most of it because the cables from detector to oscilloscope require a relatively long time to return to zero after a signal pulse.

PS intensity per bunch, as the proton intensity will vary on a bunch-to-bunch basis.

8.3 Bunch resolution

Figure 8.1 shows one diamond signal (Left 20 degrees) from a PS extraction with the mercury target in place. As anticipated, the rise time is very short and there is no problem to distinguish the individual bunches and the signal comes close to zero between two bunches. The ACEM behind the dump behaves slightly differently (fig 8.3), with a very long tail after the last bunch that takes several hundred microseconds to drop back to zero again.

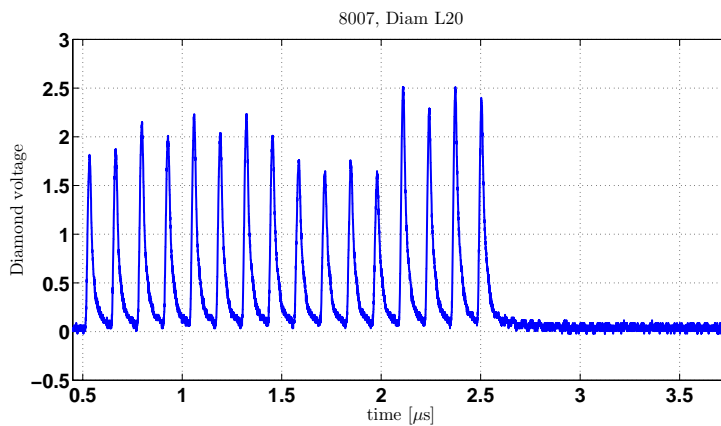


Figure 8.1. Signal from the diamond placed left of the beam dump close to the wall during a PS extraction with mercury jet.

The variations in peak amplitude can partly be explained by bunch-to-bunch variations in the PS machine (see figure 8.2). Other factors could be that the beam position changes slightly from bunch to bunch or that the diamond properties over a full extraction are not stable. Ideally, one would like to normalize the integration of each bunch to the signal from the current transformer as a confirmation that the diamond signal can be trusted, but for reasons not fully understood there is a lot of ringing between the micro bunches that makes it difficult to get a better bunch intensity accuracy than some ten percent.

8.4 Equipment scan using particle detectors

A few meters upstream of the target system are two beam monitors displaying the position of the proton beam after a PS extraction. But, as mentioned earlier, there is no way of directly telling that the beam is in its right position inside the solenoid, other than trusting that the target system is well aligned with the two beam monitors. Early during the run, we suspected that there was a misalignment

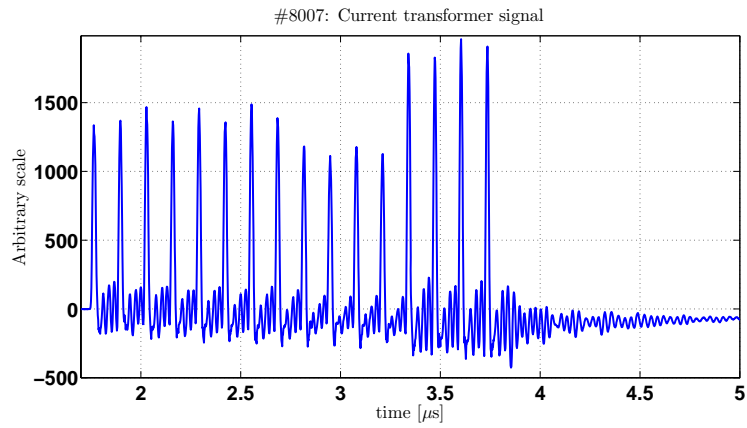


Figure 8.2. The current transformer response.

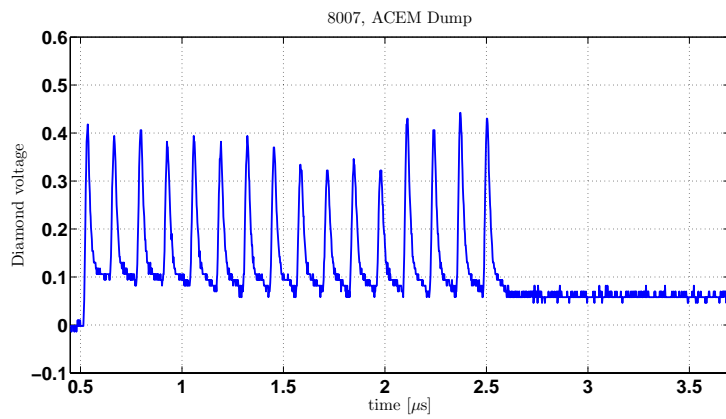


Figure 8.3. Signal from the ACEM behind the beam dump during a PS extraction with mercury jet.

of these parts. To verify this, we performed a horizontal and vertical scan with the beam on the target system but without any mercury. By looking at the yield of secondary particles for each beam position (relative to the monitors), we were able to see whether the beam interacted with more or less material. When the beam is in the right position and there is no mercury jet, the proton beam should in principle have a clear way through the target system, apart from the two thin titanium beam windows (the system is designed to have as many protons as possible interacting with the mercury and not the containment vessels). So, by sweeping the beam in the horizontal and vertical plane and looking at the integrated detector signal, we hoped to find a “valley” corresponding to a passage through the beam windows.

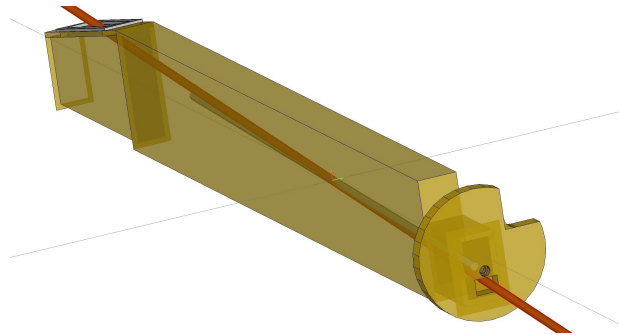


Figure 8.4. The mercury container with the two titanium beam windows. Beam is represented as a long red rod.

All diamonds confirm that indeed there is a minimum point around -14 millimeters (horizontal coordinate). Even the width and height of this valley corresponds to the dimensions of the beam window. As a confirmation, the ACEM detector that is positioned behind the dump right on the beam line, shows a maximum at the same coordinates, which is what one would expect as this detector in principle sees the particles that have not been scattered inside the solenoid, as opposed to the other. Based on this, we define the region between -20 and -10 millimeters in the horizontal plane and +2 and -8 millimeters in the vertical plane as the “scan valley”. Inside this region, the fluctuations due to different beam position should be minimal.

8.5 Linearity

To verify that the diamonds behave linearly, i.e. that the integrated signal per proton is independent of the beam intensity, several PS extractions at different intensities with no mercury jet were made. Intensity can be varied by changing the number of bunches or the the number of protons per bunch.

As seen in figures 8.7 and 8.8, there is no clear trend of deviating from a linear fit, although there are some fluctuations. But since the fluctuations follow the same pattern for all diamond detectors, even though the difference in MIPs per diamond

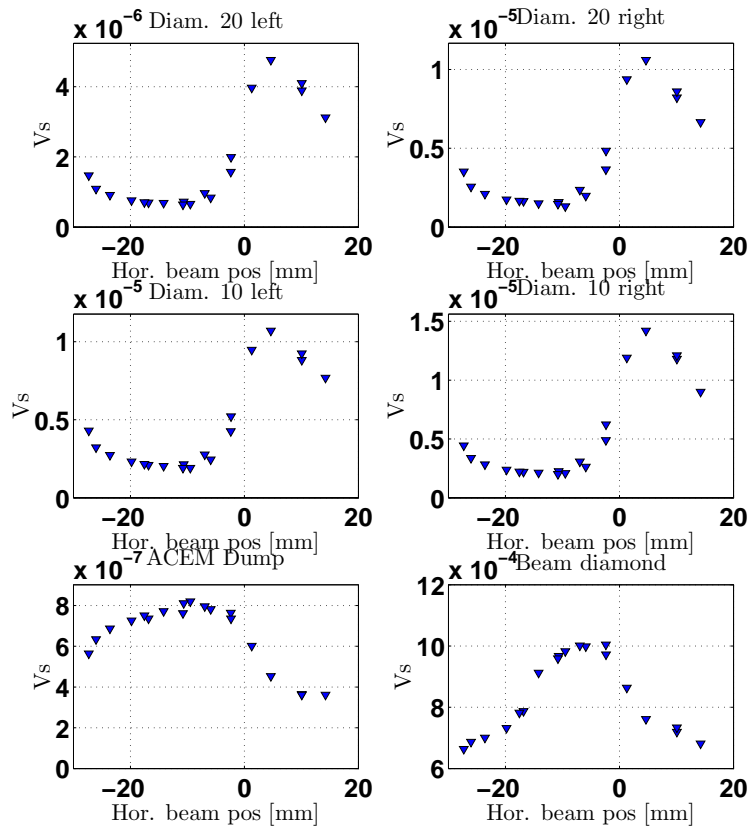


Figure 8.5. Horizontal scan. Integrated signal vs. horizontal beam position.

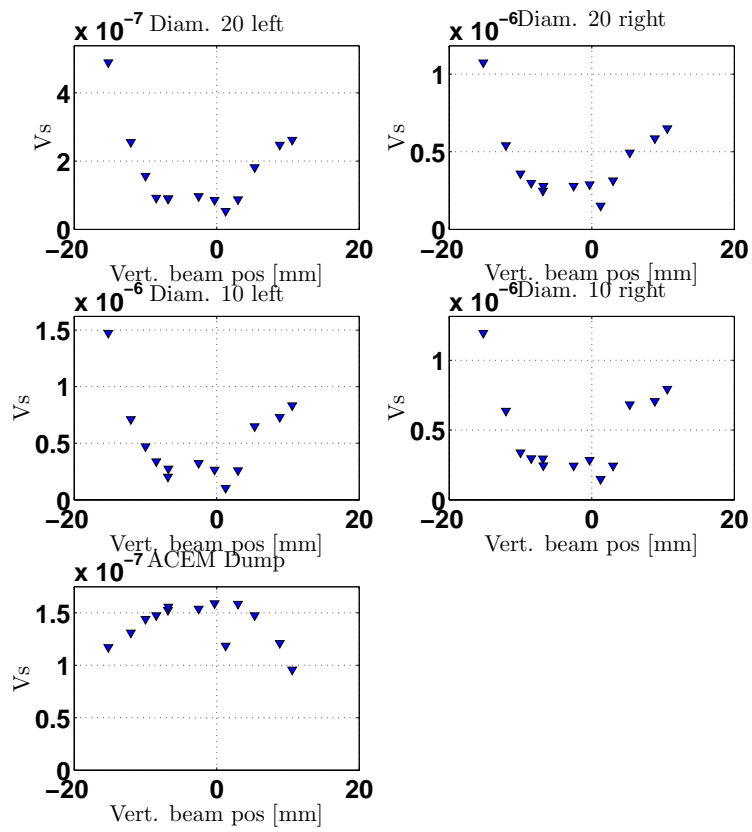


Figure 8.6. Vertical scan. Integrated signal vs. beam position.

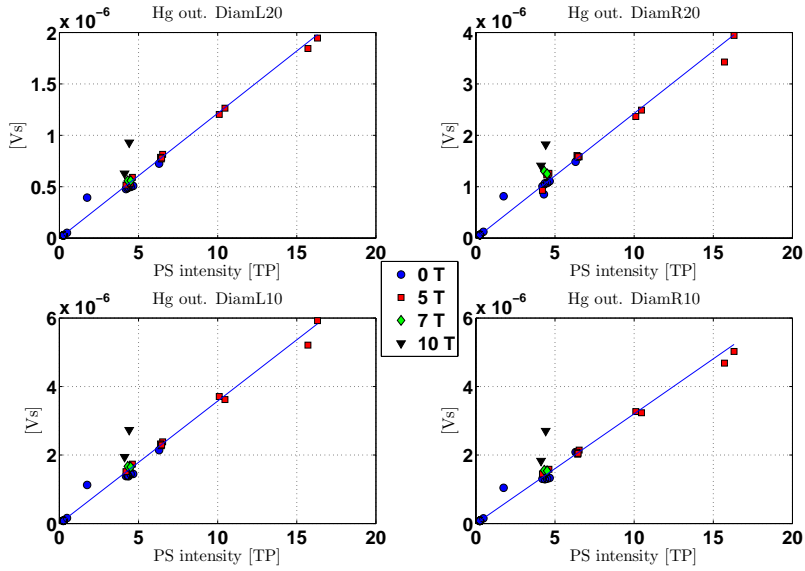


Figure 8.7. Integrated signal vs beam intensity at different magnetic fields. Beam positions are inside “scan valley” and there is no target.

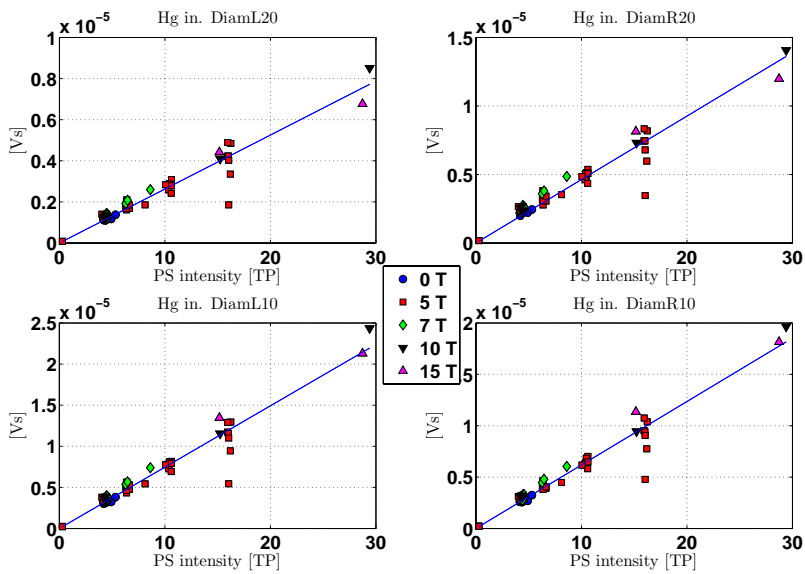


Figure 8.8. Integrated signal vs beam intensity at different magnetic fields. Beam positions are inside “scan valley” and mercury jet is in.

ranges over a factor of three from the left 20 degree and the dump diamonds, it seems unlikely that this is solely due to a non-linear saturation phenomenon of the diamond. With mercury target in we see some very large fluctuations in the integrated signal at around 15 TP. This indicates that the target position or beam impact point can change a lot from time to time.

8.6 Target in and out ratio

A comparison of the simulated particle flux and experimental results is presented in figures 8.9 to 8.11 (taking only data with a beam position in the scan valley and no-probe runs from the 24 GeV/c extractions). The flux of charged particles is calculated using:

$$\Phi = \frac{1}{Rq_e N} \frac{1}{36 \cdot 500} \cdot \frac{1}{\delta/d} \cdot \frac{1}{A} \int U(t) dt \quad [\text{MIPs/cm}^2] \quad (8.2)$$

where R is the oscilloscope input impedance, N the number of beam protons, $U(t)$ the detector signal (multiplied by its attenuation), δ and d the diamond CCD and thickness and A the diamond surface area. With no target, the simulations are in agreement with the results, but with target in the measured flux is significantly lower than the simulated. Why this is the case is not evident, but part of the explanation could be a misalignment of the beam line: the first hint of this came with the horizontal and vertical scan where the minimum point was dislocated some 15 mm from the nominal beam line center. It could also be that the proton beam meets the mercury jet at an horizontal angle, which reduces the effective interaction region (or that the vertical angle is too large, with the same effect). The fact that the in-out ratio is so much lower than expected makes it somewhat cumbersome to make any definitive statements of the target system quality (since it indicates that the mercury is not subject to the amount of protons desired).

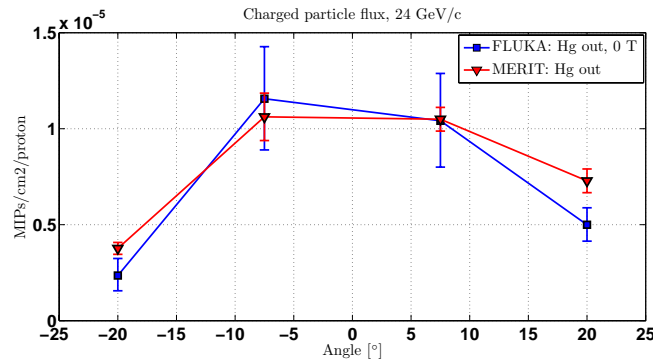


Figure 8.9. Flux of charged particles per cm^2 and proton with target out, experiment and simulations.

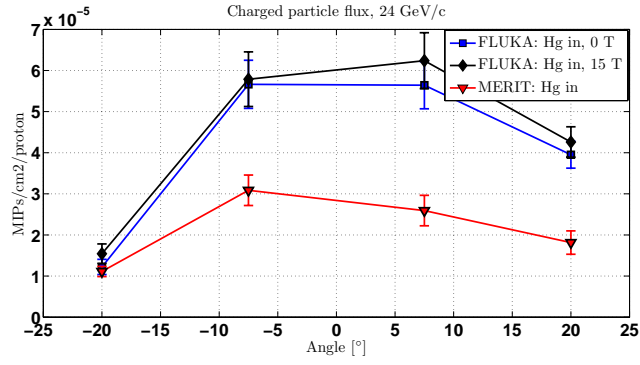


Figure 8.10. Flux of charged particles per cm² and proton with target in, experiment and simulations.

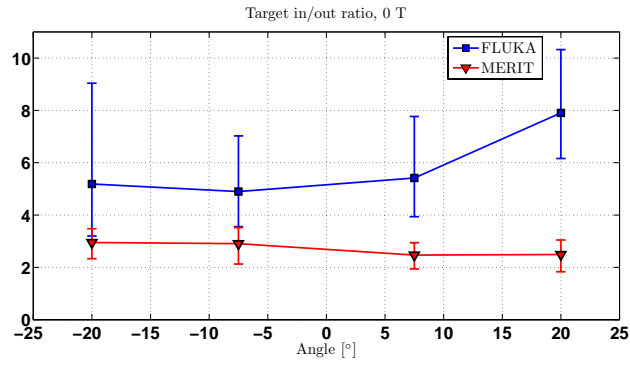


Figure 8.11. Target in and out ratio, experiment and simulations.

8.7 Probe-pump ratio

To see the behavior of the mercury jet using the pump-probe method, we look at the yield of secondary particles per proton for each of the two extraction groups (i.e. integrate the pump and probe parts of the signal and normalize to the number of protons in each group). If there is no disruption or cavitation, the yield should be the same.

We start by having a look at the quote:

$$Q = \frac{\int U_{probe} dt / N_{probe}}{\int U_{pump} dt / N_{pump}} \quad (8.3)$$

where N is the number of protons in the pump or the probe and U the detector signal. With $Q = 1$, the target system gives as many secondary particles per proton for the probe as for the pump. Initially, we look at signals with a proton beam position inside the “scan valley”. It is also important that the only parameter changing between the runs is the pump-probe time: the total extracted intensity, the beam momentum and spill structure should be constant. Presented in fig 8.12 are the results from day 8, with a beam intensity of $15 + 5$ TP, delivered in $12 + 4$ bunches for the diamond detector at 20 degrees left (the other diamonds give similar results). With the mercury target in, the trend seems decreasing up until some 50 microseconds. What is puzzling is the large variation when there is no target at all (one target-out point at $40 \mu s$ is obscured by a target-in point). This is actually of major concern since this is seen when looking at other series with other configurations and it damages the credibility when trying to make statements of the target behavior as the variations have not been found to correlate to anything else. On the other hand, the probe yield is never seen to be less than 80% of the pump yield, for spill separations up to $700 \mu s$.

In figure 8.13 from day 15, where the beam intensity is $12 + 4$ TP, the probe-pump ratios are even overlapping for target in and out, although in a narrow span of about 4 percent. The signal per proton is indeed lower for probe, but as this is the case regardless of any mercury present, one can not credit this observation to mercury cavitation.

Another interesting observation is the particle yield per bunch in the beginning and in the end of a long series of consecutive pulses. For a 16 bunch extraction, the time between first and last bunch is almost 2 microseconds. Plotted in figure 8.14 is the quote between the integrations of the first three and last three bunches², normalized to the beam intensities given by the current transformer. There is quite a clear decreasing trend for increasing beam intensities for the diamond detectors³. If this is due to mercury target cavitations growing over the course of two microseconds, one would expect to see the opposite trend for any detector placed right behind the target, in the beam line. This is supported by the ACEM detector behind the dump (same figure). But still, there are very large fluctuations for the many data points at lower intensity. Another possible explanation could

²The average over groups of three is to minimize the effects of erroneous values from the current transformer data.

³As before, the other diamonds show the same trend, but are not presented here.

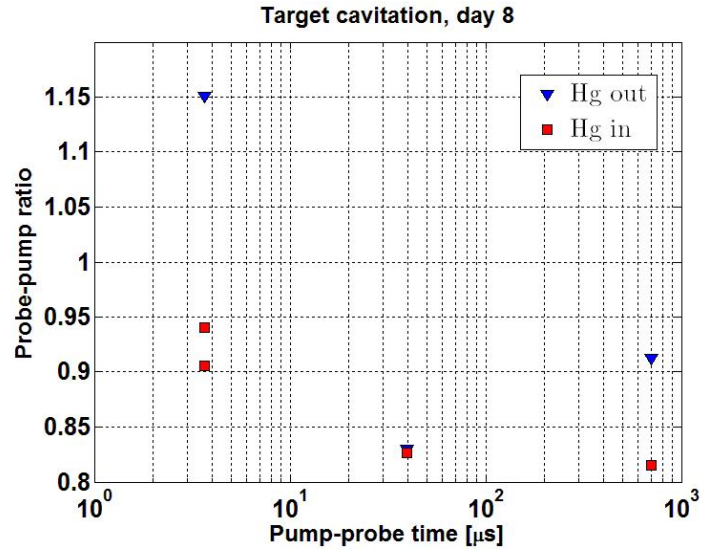


Figure 8.12. Probe-pump ratio, day 8.

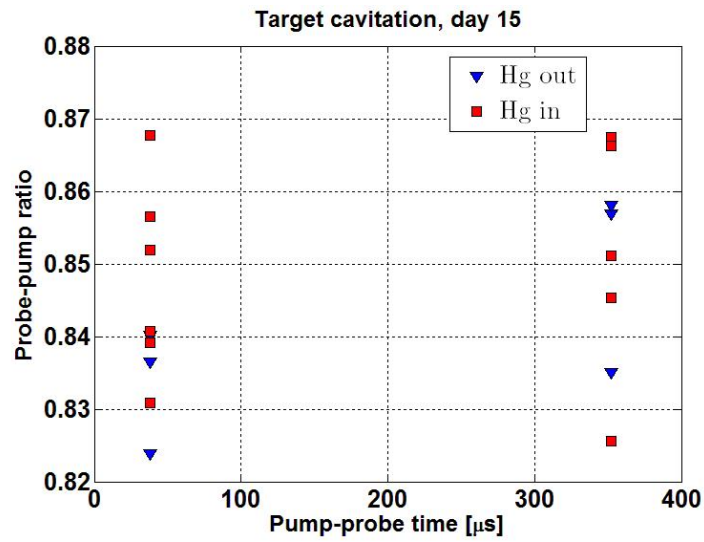


Figure 8.13. Probe-pump ratio, day 15.

be that the diamonds response weakens over time when subjected to a strong flow of particles. This is discussed in chapter 9.

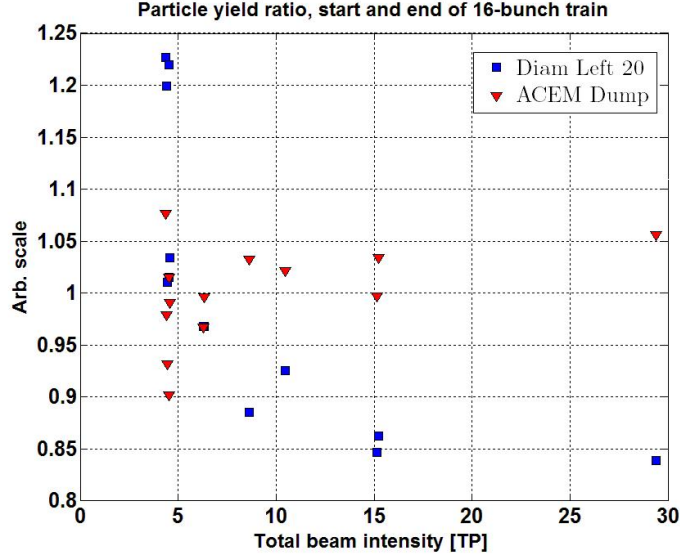


Figure 8.14. Particle production ratio, end and start of 16 consecutive bunches over 2 microseconds.

8.8 Diamond detector in beam line

One of the diamond detectors was repositioned to the beam line on top of the snout where it was subjected to a large fraction of the PS beam, having intensities of up to $3 \cdot 10^{13}$ protons distributed over 16 bunches. Although the interpretation of the response is not crystal clear, some observations are presented here.

As expected, the detector showed clear saturation behavior. In figure 8.15 we see the diamond voltage during one 16 bunch extraction. It is calculated as:

$$U_d(t) = \mathcal{F}^{-1} \left\{ \frac{U_{osc}(\omega)}{H_{cable}(\omega)} \right\} \quad (8.4)$$

with \mathcal{F}^{-1} denoting the inverse Fourier transform and U_{osc} the signal measured on the oscilloscope (multiplied with the attenuation). The voltage over the reservoir capacitor is estimated to:

$$U_C(t) = U_0 - \frac{1}{R_{osc}C} \int_0^t U_d(t') dt' \quad (8.5)$$

The first peak reaches almost 500 Volts and the falling trend of the rest indicates that the capacitor does not maintain its operating voltage. In fact, the diamond

voltage drop over the 2 microseconds is so much larger than the estimated capacitor ditto that one could be led to believe that the effective capacitive value is smaller than 100 nF.

During the first bunches, we also see a distinct peak corresponding to the 50 ns width of the PS bunches, followed by a “saddle”. Although such behavior could be modeled by having very different lifetimes for the electron and the holes, the effect vanishes after about 6 bunches.

Considering that the amount of electron-hole pairs created in the diamond is several orders of magnitude larger in this detector than any of the other, the self-screening effect of the internal charge must be taken into account for a better understanding of the signal under such extreme conditions. When the cathode and anode separate the free charge carriers, these will in turn create an electric field in the diamond opposing the externally applied and thus reducing the total field.

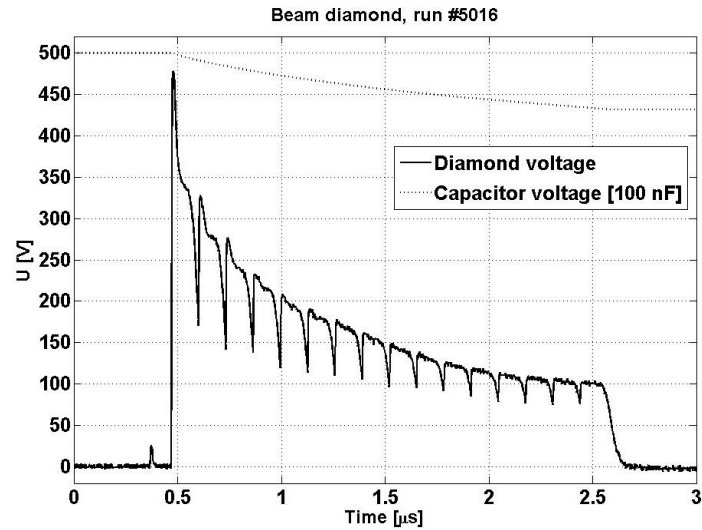


Figure 8.15. Signal from the beam diamond, corrected for cable attenuation.

Chapter 9

Conclusions

Simulations in FLUKA have confirmed previous MARS simulations of the complete MERIT setup. The detector system has been successfully used to verify these simulation results with mercury target absent. A scan of the target system interior to correct for misaligned equipment has also been made by looking at the yield of secondary particles from the proton beam when aimed at different positions.

To fully understand the detector responses, more studies of the diamonds need to be made with a reference beam under controlled forms in order to extract as much information as possible from available data.

The target has been observed to have eruption thresholds at 8 TP in harmonic 16 and 16 TP in harmonic 8. This effect was not expected, but motivates further study as it implies that one could increase the target power by a factor of two by simply changing the frequency of the proton bunches. Regardless of eruption, the particle production in the target system has not been observed to decrease by more than 20% up to 1 ms. By measuring the maximum disruption length along the mercury with the optical diagnostics, we have seen that the repeatability rate condition of 20 ms is met.

9.1 Outlook

Before the experiment, efforts were made to get beam time in order to “get to know” the diamond detectors fully, without succeeding. Now that the experimental run is finished, the results pose some questions that need to be answered. One thing that makes the analysis difficult is that one can not clearly distinguish which effects are due to mercury target behavior (position, spot size, jet shape quality etc.) and which are due to hitherto unknown diamond detector properties.

In order to have a better understanding of the results, some calibration measurements of the diamond detectors in a controlled beam are necessary. Most important is the integrated signal for a known number of protons during a short extraction, and up to which level this is linear with respect to the intensity. At present the particle flux estimation is based on single-particle responses. One could

also measure the response for a number of consecutive bunches and compare this with the decrease in figure 8.14; the same thing for pump-probe measurements.

Another effect that should be refuted, if possible, is memory behavior of the diamonds. During some days, we saw a strong correlation between the normalized detector integrals and the time that they had been allowed to “rest” after the previous beam extraction: after a longer waiting period, we had a strong signal that gradually weakened during the following shots where the magnetic field was lower than 15 Tesla, thus allowing for more than one shot without cooling. However, this was not observed most of the days and is perhaps mere coincidence. It also contradicts known diamond properties, where a diamond detector will give the most signal after it has been pumped, i.e. all the charge traps have been filled by flushing the diamond with minimum ionizing particles. Under a bias voltage, the charge traps should remain filled for days. Nevertheless, it is definitely worth investigating, all in order to isolate and compensate for effects that are not connected to the target system quality.

Several improvements have been suggested to other parts of the MERIT experiment for the possibility of a new version. On the detector side, one such change could be to reduce the thickness (and even the surface area) of the diamond samples. This can eliminate the need of signal attenuation between detector and read-out system. If above calibration measurements are satisfying the ACEM detectors can be completely left out.

Bibliography

- [1] *Journal of Physics G, Nuclear and Particle Physics*. Institute of Physics Publishing, 2006.
- [2] J. Roger J. Bennett¹, Luca Bruno, Chris J. Densham¹, Paul V. Drumm¹, T. Robert Edgecock, Adrian Fabich, Tony A. Gabriel, John R. Haines, Helmut Haseroth, Yoshinari Hayato, Steven J. Kahn, Jacques Lettry, Changguo Lu, Hans Ludewig, Harold G. Kirk, Kirk T. McDonald, Robert B. Palmer, Yarema Prykarpatsky, Nicholas Simos, Roman V. Samulyak, Peter H. Thieberger, and Koji Yoshimura. *Studies of a Target System for a 4-MW, 24-GeV Proton Beam*. Technical report, CERN-INTC, 2004.
- [3] M. Despeisse. *Etude et caractérisation d'un capteur en silicium amorphe hydrogéné déposé sur circuit intégré pour la détection de particules et de rayonnements*. PhD thesis, L'Institut National des Sciences Appliquées de Lyon, 2006.
- [4] R. Samulyak et al. *Numerical Simulation of Free Surface MHD Flows: Richtmyer - Meshkov Instability and Applications*. In *Lecture Notes in Computer Science*, volume 2331, pages 558–567. Springer-Verlag, Berlin, 2003.
- [5] A. Fasso', A. Ferrari, J. Ranft, and P.R. Sala. *FLUKA: a multi-particle transport code*. CERN 2005-10 (2005), INFN/TC_05/11, SLAC-R-773.
- [6] A. Fasso', A. Ferrari, S. Roesler, P.R. Sala, G. Battistoni, F. Cerutti, E. Gadioli, M.V. Garzelli, F. Ballarini, A. Ottolenghi, A. Empl, and J. Ranft. *The physics models of FLUKA: status and recent developments*. Computing in High Energy and Nuclear Physics 2003 Conference (CHEP2003), La Jolla, CA, USA, March 24-28, 2003, (paper MOMT005) eConf C0303241 (2003), arXiv:hep-ph/0306267.
- [7] Juan Luis Fernández-Hernando. *Development of a Beam Condition Monitor System for the Experimental Areas of the LHC Using CVD Diamond*. PhD thesis, Universitat Politècnica de Catalunya Espagne, 2004.
- [8] H. Frais-Koelbl, E. Griesmayer, H. Kagan, and H. Pernegger. *Design and test of a high-speed beam monitor*. Vienna Conference on Instrumentation, 2004.

-
- [9] S. Huss. *A Mathematical and Lumped-Element Model for Multiple Cascaded Lossy Transmission Lines with Arbitrary Impedances and Discontinuities*. Technical report, IBM, 1995.
- [10] H. Pernegger, S. Roe, P. Weilhammerb, V. Eremin, H. Frais-Kölbl, E. Griesmayer, H. Kagan, S. Schnetzer, R. Stone, W. Trischuk, D. Twitchen, and A. Whitehead. *Charge-carrier properties in synthetic single-crystal diamond measured with the transient-current technique*. *Journal of applied physics*, 2005.
- [11] Sune Söderkvist. *Tidskontinuerliga signaler och system*. Sune Söderkvist, 2000.
- [12] Nickolas Solomey. *The elusive neutrino*. 65. Scientific American library, 1997.
- [13] S. Striganov. *PARTICLE FLUX CALCULATION-III*. Technical report, Fermilab, 2006.

Appendix A

Neutrino physics

A.1 History

The first clues of the existence of the neutrino came from observing beta decay, at a time when protons, neutrons and electrons were considered the only fundamental particles¹. In this process, a neutron transforms into a proton and an electron. However, there was a problem with the energy spectrum for the electron: it seemed to imply that the conservation law of energy was violated. To get around this the famous physicist Wolfgang Pauli suggested² that there was a fourth, neutral, particle involved that balanced the energy and momentum before and after decay.

$$n \rightarrow p + e^- + \bar{\nu}_e \tag{A.1}$$

Although several experiments and observations, involving cosmic rays, had hinted of the neutrino existence, it would take until 1956 (26 years after Pauli's proposal) to get a final, convincing, confirmation of its existence. In this experiment one used (anti-)neutrinos generated in a nuclear reactor. When reacting with a neutron, they create one neutron and a positron. The latter is quickly annihilated by an electron, yielding two gammas with opposite momentums at about 0.5 MeV. The detection of two simultaneous gammas with the right energy would indicate that the following reaction had occurred:

$$\bar{\nu}_e + p \rightarrow n + e^+ \tag{A.2}$$

To increase credibility of the experiment they chose to detect the neutron as well by adding a neutron absorber - Cadmium - to the detector tank. When absorbing a neutron, the Cadmium nucleus enters an short-lived excited state which emits another gamma within a few microseconds:

$$n + {}^{108}\text{Cd} \rightarrow {}^{109}\text{Cd}^* \rightarrow {}^{109}\text{Cd} + \gamma \tag{A.3}$$

¹See [12].

²Not without reluctance, since he realized that this supposed particle would be very difficult to observe and the idea of hypothesizing something that is almost impossible to observe did not entice.

	1st	2nd	3rd
Quarks	u	s	t
	d	c	b
Leptons	e	μ	τ
	ν_e	ν_μ	ν_τ

Table A.1. The fundamental leptons and quarks.

A detection of the two opposite electron + positron photons followed by the Cadmium gamma after a few microseconds would be a reliable finger print of a neutrino reaction. After several months, they had gained enough data to convince the physics world that the neutrino truly exists. The average detection rate was about three neutrino events per hour. Comparing this with the total number of neutrinos from the reactor - $10^{12} - 10^{13}$ per cm^2 per second - and the detector volume of 200 liters gives a hint of just how elusive this particle is. Furthermore, the measured cross section for the reaction agreed with the predicted within 5 percent.

The slippery properties of the neutrino makes it useful in many astronomical areas. In the core of the sun, immense amounts of neutrinos are continuously generated from nuclear reactions. Unlike the photons also created there, the neutrinos easily escape through the outer layers of the sun (it would take one light-year of pure lead to absorb half of the neutrinos) and by detecting them we are, in a sense, directly observing the inner processes of a star. Even more important is the study of supernovae, a violent star death releasing huge amounts of energy and neutrinos.

A.2 Neutrino oscillations

While the neutrino can be employed to study other phenomena, the particle itself is by no means fully understood. It has spin $\frac{1}{2}$, thus a fermion, and belongs to the lepton group (see table A.1). At present, physicists are confident that there are only three types - or flavors - of neutrinos: the electron, muon and tau neutrino³.

However, the neutrinos possess some quite strange properties. For one thing, there is strong evidence that neutrinos oscillates from one flavor to another. This implies that they do have mass - but the mass eigenstates are not identical to the flavor state, which can be expressed as[1]:

$$|\nu_\alpha\rangle = \sum_i U_{\alpha i}^* |\nu_i\rangle \quad (\text{A.4})$$

³Experimentally verified at LEP (Large Electron Positron collider) experiments at CERN where two colliding electron and positron beams occasionally create Z^0 -particles that decay to other, easily measurable particles. By measuring how often this happens at different beam energies (and, thus, different Z^0 energies) and comparing this with the different theoretical predictions for different numbers of possible neutrino flavors one concluded that there are only three neutrino flavors.

where α denotes flavor eigenstate and i mass. The propagation of the mass eigenstates can be described with the Schrödinger equation, yielding:

$$|\nu_i(t)\rangle = e^{-i(E_i t - \vec{p}_i \cdot \vec{x})} |\nu_i(0)\rangle \quad (\text{A.5})$$

The momenta, p_i are common for all the mass eigenstates for a newly created neutrino, but the energy E_i will be different if there are any mass differences. The phase shifts over time makes it possible for a neutrino starting out as an electron flavor, ν_e , to later, with some probability, be observed as e.g. a muon neutrino, ν_μ . In the ultra relativistic case, the mass of the neutrino is much smaller than its momentum (natural units) why we make the approximation $E_i = \sqrt{p_i^2 + m_i^2} \approx p_i + m_i^2/2p_i$. Due to the high momentum (close to light speed) we can also put $t \approx L$ and the phase factor will be $e^{-i(m_i^2/2p)L}$. By inverting the unitary matrix U^* , the flavor state of a neutrino starting out as $\alpha = e, \mu$ or τ after traversing a distance L is:

$$|\nu_\alpha(L)\rangle \approx \sum_\beta \sum_i U_{\alpha i}^* e^{-i \frac{m_i^2}{2E} L} U_{\beta i} |\nu_\beta\rangle \quad (\text{A.6})$$

Doing the sums, we find that the probability of observing a flavor transition after the distance L is[1]:

$$\begin{aligned} P_{\nu_e \rightarrow \nu_\mu}(L) &= \langle \nu_\beta | \nu_\alpha(L) \rangle = \\ &= \delta_{\alpha\beta} - 4 \sum_{i>j} \Re(U_{\alpha i}^* U_{\beta i} U_{\alpha j} U_{\beta j}^*) \sin^2(\Delta m_{ij}^2 \frac{L}{4E}) + \\ &\quad + 2 \sum_{i>j} \Im(U_{\alpha i}^* U_{\beta i} U_{\alpha j} U_{\beta j}^*) \sin(\Delta m_{ij}^2 \frac{L}{2E}) \end{aligned} \quad (\text{A.7})$$

where $\Delta m_{ij} \equiv m_i^2 - m_j^2$. The first experimental indication of neutrino oscillations came from detecting solar neutrinos where one found the amount of electron neutrinos to be too few to account for all of the solar nuclear processes.

We have crude upper limits of the neutrino masses, but no reliable measurements have been made of any lower limit, so the possibility of massless neutrinos still remains. This would falsify the model used to explain the oscillatory behavior.

Upphovsrätt

Detta dokument hålls tillgängligt på Internet — eller dess framtida ersättare — under 25 år från publiceringsdatum under förutsättning att inga extraordinära omständigheter uppstår.

Tillgång till dokumentet innebär tillstånd för var och en att läsa, ladda ner, skriva ut enstaka kopior för enskilt bruk och att använda det oförändrat för icke-kommersiell forskning och för undervisning. Överföring av upphovsrätten vid en senare tidpunkt kan inte upphäva detta tillstånd. All annan användning av dokumentet kräver upphovsmannens medgivande. För att garantera äktheten, säkerheten och tillgängligheten finns det lösningar av teknisk och administrativ art.

Upphovsmannens ideella rätt innefattar rätt att bli nämnd som upphovsman i den omfattning som god sed kräver vid användning av dokumentet på ovan beskrivna sätt samt skydd mot att dokumentet ändras eller presenteras i sådan form eller i sådant sammanhang som är kränkande för upphovsmannens litterära eller konstnärliga anseende eller egenart.

För ytterligare information om Linköping University Electronic Press se förlagets hemsida <http://www.ep.liu.se/>

Copyright

The publishers will keep this document online on the Internet — or its possible replacement — for a period of 25 years from the date of publication barring exceptional circumstances.

The online availability of the document implies a permanent permission for anyone to read, to download, to print out single copies for his/her own use and to use it unchanged for any non-commercial research and educational purpose. Subsequent transfers of copyright cannot revoke this permission. All other uses of the document are conditional on the consent of the copyright owner. The publisher has taken technical and administrative measures to assure authenticity, security and accessibility.

According to intellectual property law the author has the right to be mentioned when his/her work is accessed as described above and to be protected against infringement.

For additional information about the Linköping University Electronic Press and its procedures for publication and for assurance of document integrity, please refer to its www home page: <http://www.ep.liu.se/>